Nucleic Acids Research, 2024, **52**, 5088–5106
https://doi.org/10.1093/nar/gkae156
Advance access publication date: 27 February 2024
Genome integrity, repair and replication

LC3B drives transcription-associated homologous recombination via direct interaction with R-loops

Junghyun Yoon[1,2,†], Yiseul Hwang[1,2,†], Hansol Yun[1,2,†], Jee Min Chung[1,2], Soyeon Kim[1,2], Gyeongmin Kim[1,2], Yeji Lee[1,2], Byoung Dae Lee[3] and Ho Chul Kang[1,2,4,*]

[1]Department of Physiology, Ajou University School of Medicine, Suwon, Gyeonggi 16499, Republic of Korea
[2]Department of Biomedical Sciences, Ajou University School of Medicine, Suwon, Gyeonggi 16499, Republic of Korea
[3]Department of Neuroscience, Kyung Hee University, Seoul 02447; Department of Physiology, Kyung Hee University School of Medicine, Seoul 02447, Republic of Korea
[4]Genomic Instability Research Center, Ajou University School of Medicine, Suwon, Gyeonggi 16499, Republic of Korea

[*]To whom correspondence should be addressed. Tel: +82 31 219 5044; Fax: +82 31 219 5049; Email: hckang@ajou.ac.kr
[†]The first three authors should be regarded as Joint First Authors.

Abstract

Exploring the connection between ubiquitin-like modifiers (ULMs) and the DNA damage response (DDR), we employed several advanced DNA damage and repair assay techniques and identified a crucial role for LC3B. Notably, its RNA recognition motif (RRM) plays a pivotal role in the context of transcription-associated homologous recombination (HR) repair (TA-HRR), a particular subset of HRR pathways. Surprisingly, independent of autophagy flux, LC3B interacts directly with R-loops at DNA lesions within transcriptionally active sites via its RRM, promoting TA-HRR. Using native RNA immunoprecipitation (nRIP) coupled with high-throughput sequencing (nRIP-seq), we discovered that LC3B also directly interacts with the 3′UTR AU-rich elements (AREs) of *BRCA1* via its RRM, influencing its stability. This suggests that LC3B regulates TA-HRR both proximal to and distal from DNA lesions. Data from our LC3B depletion experiments showed that LC3B knockdown disrupts end-resection for TA-HRR, redirecting it towards the non-homologous end joining (NHEJ) pathway and leading to chromosomal instability, as evidenced by alterations in sister chromatid exchange (SCE) and interchromosomal fusion (ICF). Thus, our findings unveil autophagy-independent functions of LC3B in DNA damage and repair pathways, highlighting its importance. This could reshape our understanding of TA-HRR and the interaction between autophagy and DDR.

Graphical abstract

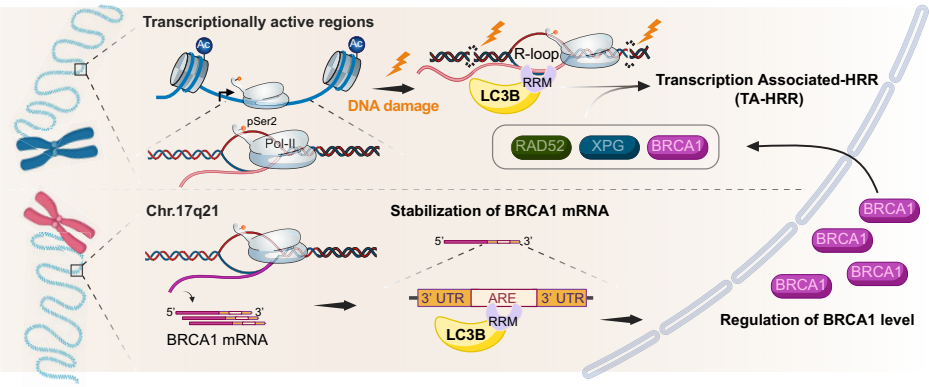

Introduction

Double-strand breaks (DSBs) represent the most severe form of DNA damage. Left unrepaired, they can induce cell death and result in genomic instability, subsequently contributing to disorders and carcinogenesis (1–3). In response, organisms have evolved DNA damage response (DDR) mechanisms, encompassing cell cycle checkpoints and repair systems (4,5).

In eukaryotic cells, DSBs are primarily mended through homologous recombination repair (HRR) and non-homologous end joining (NHEJ) (6–8). Importantly, transcription-associated (TA) repair pathways, TA-Homologous Recombination Repair (HRR) and TA-End Joining (EJ), are vital for ensuring precise DSB repair in transcriptionally active genomic regions (9,10). Such pathways are instrumental in safeguarding essential genomic segments from damage.

Received: November 9, 2023. **Revised:** February 15, 2024. **Editorial Decision:** February 15, 2024. **Accepted:** February 19, 2024

The regulation of DSB repair is deeply influenced by post-translational modifications (PTMs) like phosphorylation and ubiquitination, which modulate DDR protein function (11,12). Beyond ubiquitin, there exist over 12 ubiquitin-like modifiers (ULMs), including NEDD8, SUMO1 and LC3, with the latter being a central component of autophagy (13–15). These ULMs are implicated in a range of cellular processes, encompassing both DDR and autophagy (16–18).

Intriguingly, contemporary studies underscore the significance of autophagy in DDR. Autophagy-deficient tumor cells exhibit increased genomic instabilities, and disrupting autophagy compromises DSB repair pathways (19–22). Notably, factors such as LC3, a member of the mammalian ATG8 gene family, are pivotal in this context. Recent insights have expanded our understanding of LC3's roles, showcasing its functions in both the cytoplasm and the nucleus and illuminating its contribution to nucleophagy and genomic stability (23).

Here, we present evidence suggesting that the autophagy regulator LC3B contributes to maintaining chromosomal stability, specifically through its involvement in TA-HRR, a particular subset of HRR pathways. LC3B is summoned to DSB sites in an R-loop-dependent fashion, boosting BRCA1's recruitment and facilitating TA-HRR. Concurrently, LC3B influences the stability of *BRCA1* mRNA. Collectively, our results spotlight the pivotal role of LC3B in upholding genomic integrity, particularly within transcriptionally active areas of DNA, underlining its significance in BRCA1-mediated TA-HRR.

Materials and methods

Human cell lines

The U2OS cell line was purchased from American Type Culture Collection (ATCC, Cat.HTB-96). U2OS 2–6–3 and 2–6–5 reporter cell lines were generously provided from Dr Roger A. Greenberg (24). The DIvA- and AID-DIvA-U2OS cell lines (Stably expressing AsiSI-ER) were generously provided from Dr. Gaelle Legube (25). These cell lines were maintained in Dulbecco's Modified Eagle's Medium (DMEM; GIBCO, Cat. 11995-065) supplemented with 10% (v/v) fetal bovine serum (FBS; GIBCO, Cat.16000–044) and 1% penicillin and streptomycin (Pen/Strep; GIBCO, Cat. 15140122). For AsiSI-dependent DSB induction, cells were treated with 300 nM 4-OHT (Sigma, Cat. H7904) for 4 h. For indole-3-acetic acid (IAA, Sigma, Cat.I5148) treatment experiments, 4-OHT-treated cells were washed three times in prewarmed phosphate-buffered saline (PBS) and further incubated with 500 μg/ml IAA for 2 h. U2OS-based HR and NHEJ reporter cells (U2OS-DR-GFP and U2OS-EJ5-GFP) were kindly provided by Dr Jeremy Stark (26) and maintained in DMEM without sodium pyruvate (GIBCO, Cat.11965-092) with 10% (v/v) FBS and 1% Pen/Strep supplementation. The RPE-hTERT cell line was gratefully received from Dr. Kiyoshi Miyagawa (9) and maintained in DMEM/F12 supplemented with 10% (v/v) FBS. All cell lines were cultured at 37°C in a 5% CO_2 humidified atmosphere. Detailed information on cell lines used in this study is available in Supplementary Table S1.

Plasmids, siRNAs and oligonucleotides

Information on plasmids used in this study is provided in Supplementary Table S2. The sequences of siRNAs and oligonucleotides used in this study are listed in Supplementary Tables S3, S4 and S5, respectively. Cells were transfected with siRNAs using Lipofectamine RNAiMax (Invitrogen, Cat.13778150) or with plasmids using Lipofectamine 2000 (Invitrogen, Cat.11668-019), following the manufacturer's instructions.

Live and fixative cell imaging with laser micro-irradiation (m-IR)

For screening of DDR-associated ULMs, U2OS cells grown on glass-bottom dishes (SPL, Cat.200350) were transfected with 2 μg of expression vectors with the indicated GFP-tagged proteins using Lipofectamine 2000. Transfected cells were incubated with 10 μM of 5-bromo-2′-deoxyuridine (BrdU, Calbiochem, Cat.203806) for at least 36 h. Thereafter, cells were exposed to an ultraviolet-A laser (405 nm) for 1 sec (16 lines/sec) in a temperature-controlled chamber (37°C, 5% CO_2). Laser output set to 100% and 5–10 iterations with a 60× oil object was used for induction of DNA damage. For live cell imaging, images were taken every second up to 300 s after laser-induced DNA damage and then analyzed. For endogenous LC3B imaging, about 15 min post-mIR, cells were fixed with 4% paraformaldehyde (PFA, Sigma-Aldrich, Cat.P6148) for 15 min at room temperature (RT). Cells were then washed with PBS and permeabilized with 0.5% Triton X-100 in PBS for 15 min at RT. Non-specific signals were blocked with 1% bovine serum albumin (BSA) and 0.5% Triton X-100 in PBS for 1 h at RT. Primary antibodies diluted in buffer used for blocking were incubated with cells overnight at 4°C. Following this, cells were washed three times with PBS and incubated with secondary antibodies linked to Alexa fluorescence dye for 1 h at RT. After washing, nuclei were stained using 1 μg/ml of 4′,6-diamidino-2-phenylindole (DAPI, Sigma-Aldrich, Cat.D9542) in PBS for 10 min at RT. Afterward, cells were washed with PBS and mounted onto glass slides using Vectashield mounting medium (Vector Labs, Cat.H-1000). Antibodies used are listed in Supplementary Table S6. Images were obtained under a Nikon A1R confocal microscope and analyzed using NIS-element AR software (Nikon).

Monitoring the recruitment of proteins to FokI-induced DSBs

To monitor the recruitment of proteins to DNA DSBs, target plasmids were separately or co-transfected with the indicated siRNAs into U2OS 2–6–3 reporter cells integrated with Lac operator repeats (X256) in 35-mm glass-bottom dishes along with mCherry-LacI-FokI endonuclease plasmid. Cells were incubated at 37°C in a 5% CO_2 humidified atmosphere for 48 h. To stain nuclei of GFP-tagged proteins in live cells, cells were incubated with 200 ng/ml of Hoechst 33342 (Invitrogen, Cat.H3570) for at least 4 h at 37°C in a 5% CO_2 humidified atmosphere. For the accumulation of endogenous proteins at FokI-induced DSBs, cells were transfected with mCherry-LacI-FokI and subjected to immunofluorescence as described above. To observe the translocation of indicated proteins after RNase treatment, cells were permeabilized with 2% Tween-20 in PBS for 10 min at RT and incubated with 1 mg/ml of RNase A (MN, Cat.740505) or 5 units of RNase H (NEB, Cat.M0297L) in PBS for 15 min at RT. The effect of RNase A and H were observed in live cells. To observe the movement of LC3B, the following chemicals, which inhibit key factors of DSBs repair, were used: PJ34 (Santa Cruz Biotechnology, Cat. sc-204161), Olaparib (Avention, Cat. 200517-5), KU55933 (Sigma-Aldrich, Cat. SML1109), and NU-7026

(Selleck, Cat. S2893). These chemicals were administered at 10 μM for 6 h, and VE-821 (Sigma-Aldrich, Cat. SML1415) was administered at 5 μM for 18 h, to cells expressing GFP-LC3B before imaging. Other chemicals that activate or inhibit autophagy were incubated with cells as follows. Autophagy activators were used at 50 μM for 6 h (Perifosine, Sigma-Aldrich, Cat.SML0612), 1 μM for 3 h (PP242, Sigma-Aldrich, Cat.475988), 1 μM for 6 h (Rapamycin, Santacruz, Cat.sc-3504), 10 μM for 6 h (SAHA, Sigma-Aldrich, Cat.SML0061), 1 μM for 3 h (Torin1, Sigma-Aldrich, Cat.475991), and 10 μM for 6 h (TSA, Sigma-Aldrich, Cat.T8552). Autophagy inhibitors were used at 10 nM for 6 h (Bafilomycin A1, Sigma-Aldrich, Cat. 19-148), 50 μM for 6 h (chloroquine, Sigma-Aldrich, Cat.C6628) and 20 μM for 2 h (LY294002, Sigma-Aldrich, Cat. L9908). For inhibition of transcription, DRB and flavopiridol were administered for 15 h at 200 or 1 μM, respectively. Imaging for the FokI assay of GFP-tagged or endogenous proteins was carried out using a Nikon confocal microscope. Image acquisition and processing were performed using NIS-element AR (Imaging Software of Nikon A1R). To quantify any remaining signals from proteins at FokI sites, the nucleic region was selected using the annotations and measurements menu of NIS-element AR and defined as an area of interest. The percentage of remaining signals from proteins at FokI site was quantified using the following formula:

$$\% = \frac{\sum \left\{ \frac{\text{Ssample(n)}}{\text{b(n)}} / \frac{\text{Msample(n)}}{\text{b(n)}} \right\}}{\sum \left\{ \frac{\text{Sctrl (n)}}{\text{b(n)}} \right\} / \left\{ \frac{\text{Mctrl (n)}}{\text{b(n)}} \right\}} \times 100$$

where S is the protein signal intensity of the selected area; b is the background signal intensity; M is the mCherry-FokI signal intensity; and sample is the value of treated samples, and ctrl is the value of untreated or control samples. For each measurement level, at least 10 cells were used to eliminate variations in staining and image acquisition.

HR and NHEJ repair assay

The repair efficiency of HR and NHEJ were assessed using the U2OS GFP reporter cell lines U2OS-DR-GFP (HR) and U2OS-EJ5-GFP (NHEJ). To evaluate these efficiencies, reporter cells were plated in 12-well dishes and transfected with the specified siRNAs using Lipofectamine RNAiMAX. For the epistatic analysis of TA-HRR, the indicated siRNAs were either transfected individually or co-transfected with plasmids into cells using Lipofectamine RNAiMAX or Lipofectamine 2000, respectively. After 16 h, I-SceI endonuclease was delivered to reporter cells. To quantify the restoration efficiency of LC3B knocked-down cells, Flag-tagged LC3B WT or its mutants were co-transfected with siRNA targeting LC3B using Lipofectamine 2000 prior to the introduction of I-SceI. After 72 h, cells were trypsinized and centrifuged at 3500 rpm for 5 min. Subsequently, cells were washed with PBS and resuspended in the same buffer. The cell suspension was then transferred to 5-ml round-bottom polystyrene tubes (Falcon) for analysis. GFP-positive cells were quantified using a FACSAria III (BD Biosciences).

Clonogenic cell survival assay

The sensitivity of cells to ionizing radiation or drug treatment was assessed using a colony-forming assay. Cells were initially transfected with the designated siRNAs. After 24 h, they were collected and seeded into 6-well plates in triplicate (NUNC) at a density of 2.5×10^3 cells per well. The next day, cells were treated with ionizing radiation using a gamma cell irradiator (Cisbio, IBL437C) or with Olaparib (Avention, Cat. 200517–5). Subsequently, cells were incubated in a temperature-regulated chamber (37°C, 5% CO_2) for 10–14 days. Colonies were then fixed using 4% paraformaldehyde (PFA) and stained with 0.5% crystal violet (Sigma, C3886) for 30 min. The areas of the colonies were counted and analyzed using ImageJ software (National Institutes of Health).

Immunofluorescence

To analysis TA-HRR-associated foci, U2OS and RPE-hTERT cells were plated on glass-bottom dishes (SPL) and grown in the presence or absence of 200 μM of DRB. After 7 h, cells were treated with 200 ng/ml of neocarzinostatin (NCS) and incubated at 37°C for the indicated durations to induce DSBs. For staining of RPA foci, cells were pretreated with CSK buffer (10 mM Pipes, pH 7.0, 100 mM NaCl, 300 mM sucrose and 3 mM $MgCl_2$) containing 0.7% Triton X-100 and 0.3 mg/ml RNase A for 6 min. They were then fixed with 2% PFA in CSK buffer (detergent-free) for 10 min at RT. Staining of BRCA1 and RAD51 foci was performed were pre-treated with CSK buffer for 5 min and then fixed with 4% PFA in PBS for 10 min at RT. Subsequent to fixation, cells were permeabilized for 5 min with PBS containing 0.2% Triton X-100 and washed with PBS. Non-specific signals were blocked using 0.1% Tween-20 and 5% BSA in PBS at RT for 1 h. To analyze γH2AX levels, cells were treated with 200 ng/ml of NCS and fixed with 4% PFA at RT for 15 min. The fixed cells were permeabilized for 15 min with PBS containing 0.5% Triton X-100 and washed with PBS. Blocking of non-specific signals was performed with 0.5% Triton X-100 and 5% BSA in PBS at RT for 1 h. Primary antibodies, diluted in the blocking solution, were added to the cells and incubated for 1 h at RT. Afterward, the cells were washed and treated with Alexa Fluor-conjugated secondary antibodies at RT for 2 h. After a wash with PBS, cells were incubated with 1 μg/ml of DAPI in PBS at RT for 10 min. Cells were then washed with PBS and mounted onto glass slides using Vectashield mounting medium (Vector Labs). Details of the antibodies used are provided in Supplementary Table S6. Imaging was performed under a Nikon A1R confocal microscope.

Immunofluorescence for DNA/RNA hybrids

To stain DNA/RNA hybrids, we modified the protocol described by Lisa Prendergast et al. (27) Cells were fixed in ice-cold methanol overnight at –20°C. The following day, cells were washed with PBS and permeabilized using 0.1% Triton X-100 in PBS for 5 min at RT. After washing with PBS, permeabilization was quenched with 50 mM NH_4Cl for 10 min at RT. Cells were then blocked in a solution of 3% BSA and 0.1% Triton X-100 in PBS for 30 min at RT. The S9.6 antibody (Millipore, MABE1095) was applied at a 1:200 dilution in a solution of 1% BSA and 0.1% Triton X-100 in PBS overnight at 4°C. After incubation, cells were washed three times with 0.05% PBST and then treated with the secondary antibody, Alexa Fluor 488 goat anti-mouse IgG conjugate, at a 1:250 dilution for 1 h at RT. Subsequently, nuclei were stained using 1 μg/ml of DAPI in PBS for 10 min at RT. After a final set of three washes with PBS, the cells were mounted onto glass slides using Vectashield mounting medium (Vector Labs). Im-

ages of the stained cells were captured under a Nikon AlR confocal microscope.

Immunofluorescence for newly synthesized RNAs

Cells were seeded on a glass-bottom dish (SPL) and, after 24 h, treated with 200 μM of DRB for 15 h, followed by incubation for 3 h with 1 mM 5-ethynyl uridine (5-EU, Invitrogen). Newly synthesized RNAs were visualized following use of a Click-iT™ RNA Alexa Fluor™ 488 Imaging Kit (Invitrogen), with the procedure followed as per the manufacturer's instructions. To stain the nuclei, cells were treated with DAPI in PBS at RT for 10 min. Finally, cells were mounted onto glass slides using Vectashield mounting medium (Vector Labs), and images were captured under a Nikon A1R confocal microscope.

Purification of recombinant LC3B WT, RBM and HBD from sf9 and *Escherichia coli*

pENTRY vectors containing LC3B WT or mutant were transferred into the pDEST20 vector using a Gateway LR cloning system. To generate recombinant baculovirus, DH10Bac *Escherichia coli*, which contained a baculovirus shuttle vector (bacmid), was infected with pDEST20 plasmids. Purified bacmid DNA was transfected into Sf9 insect cells using Cellfectin® II Reagent (Invitrogen). After 3 days, Sf9 cells were collected and lysed with NETN buffer (25 mM Tris–HCl, pH 8.0, 150 mM NaCl, 1 mM EDTA, 1 mM DTT, 1% NP-40, 0.1% Triton X-100, protease inhibitor cocktail, and 1 mM PMSF). Soluble protein extracts were obtained by centrifugation at 14 000 rpm and 4°C and incubated with Glutathione Sepharose 4B resin (GE Healthcare Life Science) according to the manufacturer's manual. The resin was washed with NETN buffer, and then bound proteins were eluted with elution buffer (50 mM HEPES, pH 7.5, 40 mM reduced glutathione, 100 mM NaCl, 30% glycerol and 0.03% Triton X-100). Protein concentrations were determined using the Bradford method (Bio-Rad). For purification of GST-V5-LC3B WT, mutant, and HBD, the pDEST15 vector was transformed into BL21pLys and purified as we described previously (28). To obtain GST-free proteins, GST-fusion proteins derived from pDEST15-3C were incubated with HRV 3C protease (GE Healthcare) in cleavage buffer (50 mM Tris–HCl pH 7.4; 150 mM NaCl; 1 mM EDTA; 1 mM DTT) at 4°C for 24 h. The cleaved protein was purified by passing through a GST column that has an affinity for the HRV 3C protease and GST tag. The purity of the final product was examined by Coomassie brilliant blue staining, followed by electrophoresis on an 8−16% gradient SDS-PAGE. Detailed information of all reagents and proteins used in this study is available in Supplementary Tables S7 and S8.

In vitro R-loop and hybrid binding assay by EMSA

To generate R-loop, hybrids, and other control oligonucleotides such as dsDNA, dsRNA, ssDNA and ssRNA, the annealing protocol described by Risa Kitagawa *et al*. was performed (29) Briefly, probes were diluted to 0.3 nM in buffer H (50 mM Tris at pH 7.5, 10 mM $MgCl_2$, 100 mM NaCl, and 1 mM DTT). Thermal cycler conditions included a decremental temperature profile, starting from 95°C and ending at 25°C, with a 0.1°C decrease every 15 s. For the EMSA analysis, 6 pmol of each annealed probe, including R-loop and hybrids, were incubated with recombinant V5-LC3B WT, R68-70A, or HBD protein in reaction buffer (100 mM KCl, 10mM Tris, pH8.0, 1 mM EDTA, 4% glycerol, 0.1% NP-40) at RT for 1 h. For the super-shift assay, the indicated antibodies were also incubated with each sample. Anti-LC3B antibody was used, as well as Ig-G and anti-S9.6 antibodies for negative and positive controls, respectively, of R-loop binding. To exclude contamination by other proteins, LC3B WT was pre-incubated with 50 or 100 mM DTT or β-ME for 30 min at RT before mixing with a probe. After pre-electrophoresis of 5% TBE gel with 120 V, 6 × loading dye was added to each sample, and then samples were electrophoresed at 120 V for 40 min. The Cy5-labeled probe signals were visualized using an Odyssey CLx (LI-COR) at a wavelength of 700 nm. Probes employed for EMSA are detailed in Supplementary Table S5.

Comparison of LC3B structure via RCSB Protein Data Bank (RCSB PDB)

To characterize the structural similarities between LC3B and other proteins, the RCSB PDB web server was used. The published structure of LC3B was discovered by searching the structure similarity tool. Structural similarity of LC3B (PDB: 1V49, chain A) with *E. coli* RNase H1 (PDB: 1WSH, chain A) was determined using the jFATCAT (flexible) method in the Pairwise Structure Alignment menu of RCSB PDB.

Chromatin immunoprecipitation (ChIP)

ChIP assays were performed using EZ-ChIP kits (Millipore) according to the protocol described by Shanbhag *et al*. (24) Briefly, site-specific DSBs were induced in DIvA cells using 1 μM 4-OHT for 4 h. After 48 h of transfection with the indicated plasmids or siRNAs, cells were crosslinked for 15 min using 1% PFA and then quenched with glycine. Cells were then lysed in SDS buffer and sonicated. After centrifugation, the supernatants were incubated overnight with 2-μg aliquots of the primary antibodies. Antibody-bound protein/DNA complexes were then pulled down using protein G beads (Milipore), eluted and digested with protease K. The purified DNA samples were analyzed by qRT-PCR for active or inactive DSB sites. Details regarding primers and primary antibodies utilized can be found in Supplementary Tables S4 and S6, respectively. Quantitative PCR was performed using a CFX96 instrument (Bio-Rad) according to the manufacturer's instructions.

DNA/RNA-immunoprecipitation (DRIP)

DNA/RNA immunoprecipitation (DRIP) was performed with enzymatically digested DNA from DIvA cells. Cells were treated with 300 nM 4-OHT for 4 h, trypsinized, pelleted at low speed, and washed with PBS. Total nucleic acids were isolated using DNeasy Blood & Tissue Kits (QIAGEN) according to the manufacturer's instructions. For DRIP qRT-PCR, 50 μg of DNA was diluted in 300 μl of water, sonicated for 10 cycles (30 s on/30 s off) on the low setting using a Biorupter Pico (Diagenode). Then, 25 μg of the fragmented DNA was equilibrated to 1× RNase H buffer and treated with 50 units of RNase H (New England Biolabs, M0297L). After incubation at 37°C for 3 h, all samples, including RNase H treated controls, were equilibrated to 1× DRIP buffer (50 mM Tris pH 8.0, 5mM EDTA pH 8.0, 140 mM NaCl, 1% Triton X-100). Reserving a fraction as input, the remainder was incubated with 10 μg of the S9.6 antibody (Milipore, MABE1095) at 4°C for 6 h, followed by an overnight incubation with 40 μl of pre-washed Protein G Dynabeads in DRIP buffer at 4°C. Af-

ter extensive washing with DRIP buffer, the bound immunocomplexes were eluted with 120 μl DRIP Elution Buffer (1% SDS, 0.1 M NaHCO3) at 55°C for 20 min. The eluted samples were then subjected to nucleic acid purification using a NucleoSpin Gel and PCR Clean-up Mini kit for gel extraction (MACHEREY-NAGEL), and the DNA was eluted with 5 mM Tris–HCl (pH 8.5). The eluted DNA was analyzed by qRT-PCR using Bio-Rad SYBR Green master mix on a C1000 Touch Thermal Cycler (Bio-Rad). Primer pairs used are listed in Supplementary Table S4.

Immunoblotting

Cells were washed with PBS and lysed in Laemmli sample buffer (65.8 mM Tris–HCl [pH 6.8], 26.3% [w/v] glycerol, 2.1% SDS, 0.01% bromophenol blue, and 2-mercaptoethanol). Samples were boiled at 95°C for 10 min and loaded onto 8–16% or 15% SDS-PAGE. Separated proteins were transferred onto a nitrocellulose membrane (0.45 μm). Membranes were washed three times with 0.05% Tween 20 in PBS. For blocking, the membrane was incubated with 5% Difco skim milk in PBS containing 0.05% Tween 20 at RT for 1 h. Subsequently, membranes were incubated with the indicated primary antibodies in 1% skim milk at 4°C overnight. On the following day, membranes were incubated with the appropriate secondary antibodies in 1% skim milk at RT for 1 h. Western blotting was performed using a SuperSignal™ West Pico PLUS Chemiluminescent Substrate kit and X-ray film (AGFA). The intensities of bands were quantified using ImageJ (National Institute of Health).

Real-time quantitative PCR (RT-qPCR)

To quantify mRNA levels, target cells were harvested, and total RNA was extracted using TRIzol reagent (Invitrogen). This RNA was subsequently reverse transcribed into cDNA using a High-capacity cDNA Reverse Transcription Kit (Applied Biosystems). The synthesized cDNA was then subjected to RT-qPCR analysis using primer pairs listed in Supplementary Table S4. To validate RNA-seq data by RT-qPCR, iQ™ SYBR® Green Supermix (Bio-Rad) was used, and amplification was performed on a CFX96 instrument (Applied Bio-Rad) as per the manufacturer's guidelines.

Dot blot assay for R-loops and biotinylated RNA probes

U2OS cells were transfected with the indicated siRNAs for 48 h. To assess global or DSB-associated R-loop levels, cells were treated with 200 ng/ml of NCS for 2 h before collection. Following treatment, cells were washed with PBS and trypsinized. Genomic DNA (gDNA) containing R-loops was extracted using a DNeasy Blood & Tissue Kit (QIAGEN) according to the manufacturer's protocol. For the dot blot assay of R-loops, gDNA was diluted to a concentration of 100 ng/μl and spotted onto a positively charged nylon transfer membrane (GE Healthcare, RPN119B). Biotinylation of RNA nucleotides was performed using the Pierce RNA 3′ End Desthiobiotinylation Kit (Thermo Fisher Scientific, Cat. 20163) as per the manufacturer's guidelines. Post-biotinylation, ssRNA probes were applied to positively charged nylon transfer membranes in a concentration-dependent manner (2.5, 5 and 10 nM). Following application, both gDNA and biotinylated RNA were cross-linked using UV-C at 120 mJ/cm^2 with Stratalinker UV Crosslinker 1800 (Stratagene). For R-loop detection, the membranes were blocked with 5% Difco skim milk in PBS containing 0.05% Triton X-100 at RT for 1 h and then incubated with GST3CV5-HBD overnight at 4°C. The next day, the membranes were washed three times with PBS containing 0.05% Triton X-100. Following the washes, they were incubated with a GST antibody at RT for 1 h, washed three times, and then the secondary antibody was applied at RT for 1 h. After the final washes, the signal of R-loops was detected using a SuperSignal West Pico PLUS Chemiluminescent Substrate kit and X-ray film (AGFA). Band intensities were quantified using ImageJ (National Institute of Health). To detect biotinylated RNA probe signals, a Chemiluminescent Nucleic Acid Detection Module Kit (Thermo Fisher Scientific, Cat. 89880) was used according to the manufacturer's instructions.

Biotin-labeled RNA pull-down assay

RNA pull-down was performed with a Pierce™ Magnetic RNA-Protein Pull-Down Kit (Thermo Fisher Scientific, Cat.20164) following the manufacture's protocol. Each RNA oligo was labeled with 3′ biotin using a Pierce™ RNA 3′ End Desthiobiotinylation Kit (Thermo Fisher Scientific). Biotin-labeled RNA oligos were incubated with streptavidin magnetic beads for 30 min at RT with agitation. U2OS cell lysates or recombinants were mixed with RNA-bound beads for 1 h at 4°C with rotation. Then, the beads were collected and washed three times. RNA-associated proteins were eluted for immunoblot analysis.

nRIP coupled with high-throughput sequencing (nRIP-seq)

nRIP was conducted with a Magna Nuclear RIPTM (Native) Nuclear RNA-Binding Protein Immunoprecipitation Kit (Sigma-Aldrich, Cat. 17-10522), and nuclear interactions between LC3B and RNAs were analyzed as per the manufacturer's guidelines. In brief, 1×10^7 U2OS cells were plated to 150-mm dishes. For immunoprecipitation, 5 μg of anti-LC3B antibody (Cell signaling, 3868S) and anti-IgG antibody (Milipore, 12-370) were used to bind LC3B and as a negative control, respectively. To dissect conserved sequences for LC3B binding, a library was constructed using a SMART-Seq v4 Ultra Low Input RNA Kit for Sequencing (TakaRa) with each sample. The resulting libraries were sequenced on an Illumina NovaSeq 6000 System (Illumina, CA, USA) in 2 × 150 bp paired-end mode, yielding an average of 56.5 million reads per library. The sequencing was conducted by Theragen Bio. For validation, cDNA was synthesized from purified RNAs and used for qRT-PCR as a template. As a positive control, fibronectin (FN1) was measured. To validate whether BRCA1 was pull downed, three primer sets (Supplementary Table S4) were designed for other coding regions.

Bioinformatic analysis of the nRIP-seq DATA set

Adapter sequences were trimmed from the nRIP-seq library preparations using cutadapt v.2.8. The trimmed libraries were aligned to the hg38 human genome using the aligner STAR v.2.7.1a following ENCODE standard options with the '–quantMode TranscriptomeSAM' option for estimation of transcriptome expression levels. Gene expression estimation was performed using RSEM v.1.3.2 considering the direction of the reads, which corresponded with the library protocol option –strandedness. To normalize sequencing depths among

samples, TPM values were calculated. For metagene expression, the number of IgG and LC3B nRIP reads represented in the TSS and TES regions were visualized through plot profiles using deeptools. We determined LC3B n-RIP peak abundances by quantification with the MACS2 callpeak module enabling bypass of the shifting model. n-RIP peaks were then associated with these domains via bedtools' intersectBed. Peaks and mRNAs overlapping with a TPM greater than or equal to 1 were pinpointed for in-depth examination. HOMER was used to annotate peaks and generate a plotprofile of the LC3B n-RIP peaks. Lastly, consensus motif patterns within LC3B n-RIP peaks across mRNAs were explored utilizing RAST-peak motifs.

Surface plasmon resonance (SPR)

The binding kinetics of V5-LC3B WT to BRCA1 3′UTR RNAs were analyzed at RT on an iMSPR-ProX instrument (iCLUEBIO, Seongnam, Republic of Korea) using 100 mM KCl, 10 mM Tris–HCl (pH 7.9), 1 mM EDTA and 0.1% NP-40 as a running buffer. The BRCA1 3′UTR RNAs were immobilized on the surface of a HC1000 chip (iCLUEBIO) with up to 500 response units through amine coupling/avidin-biotin capture. Increasing concentrations of V5-LC3B WT (0.078, 0.156, 0.313, 0.625, 1.25, 2.5 and 5.0 μM, respectively) were injected onto the surface of a sensor chip at a flow rate of 50 μl/min. Then, 3 M NaCl was injected to remove the V5-LC3B from the surfaces at a flow rate of 50 μl/min. Kinetics evaluation data was obtained using a 1:1 binding model. The 1:1 binding model refers to the binding of one analyte molecule to one ligand molecule. After obtaining the association rate constant (ka) and the dissociation rate constant (kd), the equilibrium dissociation constant (KD) for evaluating affinity was determined by dividing the dissociation rate constant by the association rate constant. Curve fitting and data analysis were performed using iMSPR analysis software (Tracedrawer; iCLUEBIO).

End resection assay

To measure the efficiency of DSB end resection, we used the protocol described by Sharma et al. (30). Briefly, DIvA cells were seeded into 100-mm dishes with 1.2×10^6 cells per dish. The following day, DSBs were induced by refreshing the media with fresh media containing 300 nM 4-OHT, and the cells were incubated for 4 h. Subsequently, the cells were rinsed with 10 ml of ice-cold PBS and collected via trypsinization. The harvested cells were then washed with PBS and resuspended at 37°C in 0.6% Low Melting Point (LMP) agarose in PBS. A 50-μl aliquot of the cell suspension was dropped onto Parafilm and incubated at 4°C for 10 min to solidify. Agarose balls containing cells were carefully transferred to 1.5-ml Eppendorf tubes and incubated with 1 ml of ESP buffer (0.5 M EDTA, 2% N-lauroylsarcosine, 1 mg/ml proteinase-K, 1 mM $CaCl_2$, pH 8.0) for 20 h at 16°C with rotation. After this, the ESP buffer was removed and replaced with 1 ml of HS buffer (1.85 M NaCl, 0.15 M KCl, 5 mM $MgCl_2$, 2 mM EDTA, 4 mM Tris, pH 7.5, 0.5% Triton X-100), followed by another incubation for 20 h at 16°C on the rotary shaker. Post-incubation, the cells were washed six times with PBS at 4°C, with each wash lasting 1 h. To extract gDNA from the cells, each agarose plug was heated on a 70°C heat block for 10 min. The extracted gDNA was then diluted, and 180 ng per reaction was cleaved with 20 units of BsrGI-HF (NEB, #R3575S) restriction enzyme at 37°C for 20 h. Prior to qRT-PCR, the enzyme was deactivated by heating at 65°C for 30 min. To analyze the efficiency of end resection, 100 ng of the restricted gDNA served as the template for qRT-PCR. For qRT-PCR of gDNA, iQ™ SYBR® Green Supermix (Bio-Rad) was used, and amplification was performed on a CFX96 instrument (Bio-Rad) as per the manufacturer's guidelines. The value obtained by subtracting the Ct of the mock-digested samples from the Ct of the BsrGI-HF-digested sample was considered the ΔCt, which was used to calculate the ssDNA percentage within specific genome Chr 1: 89231183. Relevant primers are listed in Supplementary Table S4.

Sister chromatid exchange (SCE), interchromatid fusion (ICF) and chromosomal breakage assay

For analysis of SCEs, we used the protocol described by Tumini *et al.* (31). U2OS cells were plated in 100-mm dishes. After 24 h, media was replaced with media containing 10 μM of BrdU and incubated for 48 h. Afterward, cells were treated with 200 ng/ml of NCS for 12 h. Before harvest, cells were incubated with 0.1 μg/ml colcemid for at least 3 h to arrest the cells in the mitotic phase. Arrested cells were swelled with pre-warmed 75 mM KCl at 37°C in a water bath for 15 min after detachment. Swelled cells were fixed with a fixative solution consisting of methanol:acetic acid (3:1). Fixed cells were harvested by centrifugation for 5 min at 250 × g at RT. Supernatant was removed, and cells were washed with fixative solution at least 4 times. Cells were resuspended in 500 μl of fixative solution. Glass slides were cleaned up with 70% ethanol and coated with 45% acetic acid. The resuspension solution containing the cells was dropped onto glass slides from a height of 15 cm above the slides. Before staining, slides were incubated at 55°C overnight. After incubation, chromosomes were stained with 0.1 mg/ml acridine orange for 10 min at RT and washed with water. Slides were covered in 2 × SSC buffer (30 mM sodium citrate and 300 mM NaCl, pH 7.0) and exposed to ultraviolet-C irradiation for 15 min using a Stratalinker® UV Crosslinker 1800 (Stratagene). After irradiation, slides were placed in a Coplin jar and covered with pre-warmed 55°C 2 × SSC buffer. Slides were incubated at 55°C for 20 min, washed with water, and mounted with a microscope cover glass using Vectashield mounting medium (Vector Labs). For ICF and chromosomal breakage assays, except for the omission of BrdU, samples were processed using the method described for the SCE assay and then stained with 2 μg/ml of DAPI. Images were captured using a Zeiss Confocal Microscope LSM710.

Image quantification and statistical analysis

Images were taken using Nikon A1R and Zeiss LSM710 confocal microscopes. All images from each experiment were taken at the same exposure time. Quantification of images from a Nikon A1R microscope was obtained using NIS-element AR software. Images obtained from the Zeiss LSM710 were quantified by counting. The immunoblotting bands of immunoblotting were quantified using ImageJ (National Institute of Health). For the FokI analysis, recruitment signal of proteins was measured and normalized using the nuclear background signal, as outlined in the 'Monitoring the Recruitment of Proteins to FokI-induced DSBs' section. The data is expressed as the mean ± standard error of mean (s.e.m.). For the end resection analysis, we employed

the equation from Sharma et al. to calculate the percentage of single-stranded DNA (ssDNA) within a specific genome (30). The statistical analysis was performed using GraphPad Prism 8.0 (GraphPad Software, San Diego, CA, USA). Statistical significance for each experiment is described in figure legends. All softwares used in this study are listed in Supplementary Table S9.

Results

LC3B is directed to DSBs via its RNA recognition motif, modulating the HR pathway beyond autophagy

To elucidate the role of ULMs in the DDR, we employed a laser micro-irradiation (m-IR) system. Utilizing a human liver cDNA library, we isolated 12 ULMs and subsequently generated N-terminal GFP-tagged ULMs. After transfection into U2OS cells, the dynamics of these ULMs at DNA damage sites were assessed (Figure 1A and Supplementary Figure S1A). Among them, seven ULMs, notably GABARAPL2 (GBL2)—a member of the ATG8 subfamily of autophagy-related genes (ATGs) —showed significant accumulation at m-IR-derived DNA lesions, hereafter referred to as laser stripes.

Given the strong association between DDR and autophagy, we further analyzed 16 ATGs in DDR. Employing m-IR, we observed that eight ATGs, including GBL2, localized to DNA lesions, whereas ATG4D, LC3A and ATG10 showed minimal accumulations (Figure 1A and Supplementary Figure S1B). Although the m-IR system is a valuable tool for DDR research due to its ability to induce various DNA breaks, its constraints include ROS production, lipid disruption, and potential autophagy activation (32). This led us to transition to the FokI system in U2OS 2–6–3 reporter cells for precise DSB induction in the nucleus, minimizing the influence of external factors. Consequently, six ATG8 family members, especially GABARAP and LC3 variants, localized to FokI-induced DSBs, emphasizing the potential role of the ATG8 family in DDR (Figure 1A and Supplementary Figure S1C).

Within the ATG8 family, LC3B, a central component of autophagy (33), became our main subject of interest. Prior to comprehensive LC3B investigations, we first confirmed the LC3B antibody's specificity for detecting endogenous LC3B (referred to as endo-LC3B henceforth) in DDR using siRNA sets targeting both LC3B and its isoforms (Supplementary Figure S1D and E).

Concurrently, this process of confirming antibody specificity through siRNA sets allowed us to identify two siRNAs for further experimentation, underlining their targeted effectiveness. Following this preliminary step, we selected siLC3B #1 (hereafter referred to as siLC3B) from among the siRNAs, as it demonstrated the most efficient knockdown of endo-LC3B protein. To address potential off-target effects of siLC3B, we also chose an siLC3B #1 mutant (hereafter referred to as siLC3B mut), which contained three nucleotide alterations that disrupt the ability of the siRNA to target LC3B mRNA (Supplementary Figure S1D and E).

Having established the selectivity of the LC3B antibody, we proceeded to employ it in the detection of endo-LC3B's significant association with DNA lesions in the m-IR system. Notably, endo-LC3B primarily localized to DNA lesions, showing co-localization with γH2AX, a marker for DSB sites (Figure 1B). In the FokI system, both endo-LC3B and GFP-LC3B exhibited DSB-specific localization patterns (Figure 1C). Utilizing siRNA sets, we further confirmed that endo-LC3B authentically translocates to and concentrates at DSBs, underscoring its inherent relationship with DSB-associated DDR (Figure 1D and E).

Subsequently, to probe LC3B's function in genomic damage and the repair pathway, we adopted DR and EJ5 U2OS cell lines. This enabled us to monitor alterations in the NHEJ and HR mechanisms. Our findings revealed that LC3B depletion led to a reduction in HR, which, although significant, was less extensive than the major decrease seen with BRCA2 knockdown (Figure 1F). This indicates that LC3B may have a specialized or context-dependent role in HR, likely affecting a particular subset of HR pathways. RAP80, a primary NHEJ factor, was utilized as a control for gauging LC3B effects on NHEJ (Figure 1F). Following the observation of an HR defect in the LC3B-depleted condition, we investigated the repercussions of LC3B depletion on the cellular DNA damage response. Notably, we observed that LC3B knockdown led to a significant increase in γH2AX foci formation after neocarzinostatin (NCS) treatment at both 2 and 6 h. This increase, when compared to that in untreated LC3B-depleted cells, highlighted an enhanced sensitivity to NCS-induced DNA damage (Supplementary Figure S2A), a finding supported by western blot results that revealed a surge in γH2AX protein levels (Supplementary Figure S2B).

We then investigated the consequences of LC3B depletion on chromosomal stability. After NCS exposure, LC3B-depleted cells exhibited an increased rate of chromosomal anomalies, as demonstrated by chromosomal breakage analysis. This increase paralleled the rise in γH2AX, indicating that the absence of LC3B compromises DSB repair, leading to genomic instability, including that due to chromosomal breakages (Supplementary Figure S2C). Additionally, cell viability assays under ionizing radiation confirmed a significant reduction in survival of LC3B-depleted cells (Supplementary Figure S2D), reinforcing the view that LC3B plays a critical role in maintaining genomic integrity and cellular resilience in response to DNA damage.

In light of the HR deficiency observed in LC3B knockdown cells, we further investigated the sensitivity of these cells to PARP inhibitor treatment, positing that the compromised DNA repair pathways could lead to increased vulnerability. Confirming our hypothesis, LC3B-depleted cells exhibited a significant reduction in survival upon exposure to PARP inhibitors (Supplementary Figure S2E). This outcome more directly associates LC3B with HR-mediated DNA damage repair processes, emphasizing its crucial role in the maintenance of genomic stability. The gathered data imply that the absence of LC3B not only escalates DNA damage signaling and chromosomal anomalies but also heightens the sensitivity of cells to treatments targeting HR deficiencies.

To further elucidate LC3B's impact, we simulated radiation effects using NCS treatment and assessed BRCA1 foci formation, a critical event in HRR, under conditions of LC3B reduction. Our observations disclosed a considerable reduction in BRCA1 foci, paired with a decrease in RAD51 foci. These patterns coincide with those seen during RNF168 depletion, signifying LC3B's essential role in the HR DNA repair pathway (Figure 1G and H and Supplementary Figure S2F and G).

To ascertain the upstream DDR regulators that direct LC3B to sites of genomic damage, we co-expressed GFP-LC3B and mCherry-FokI in U2OS 2–6–3 cells. After a 24-h period, cells

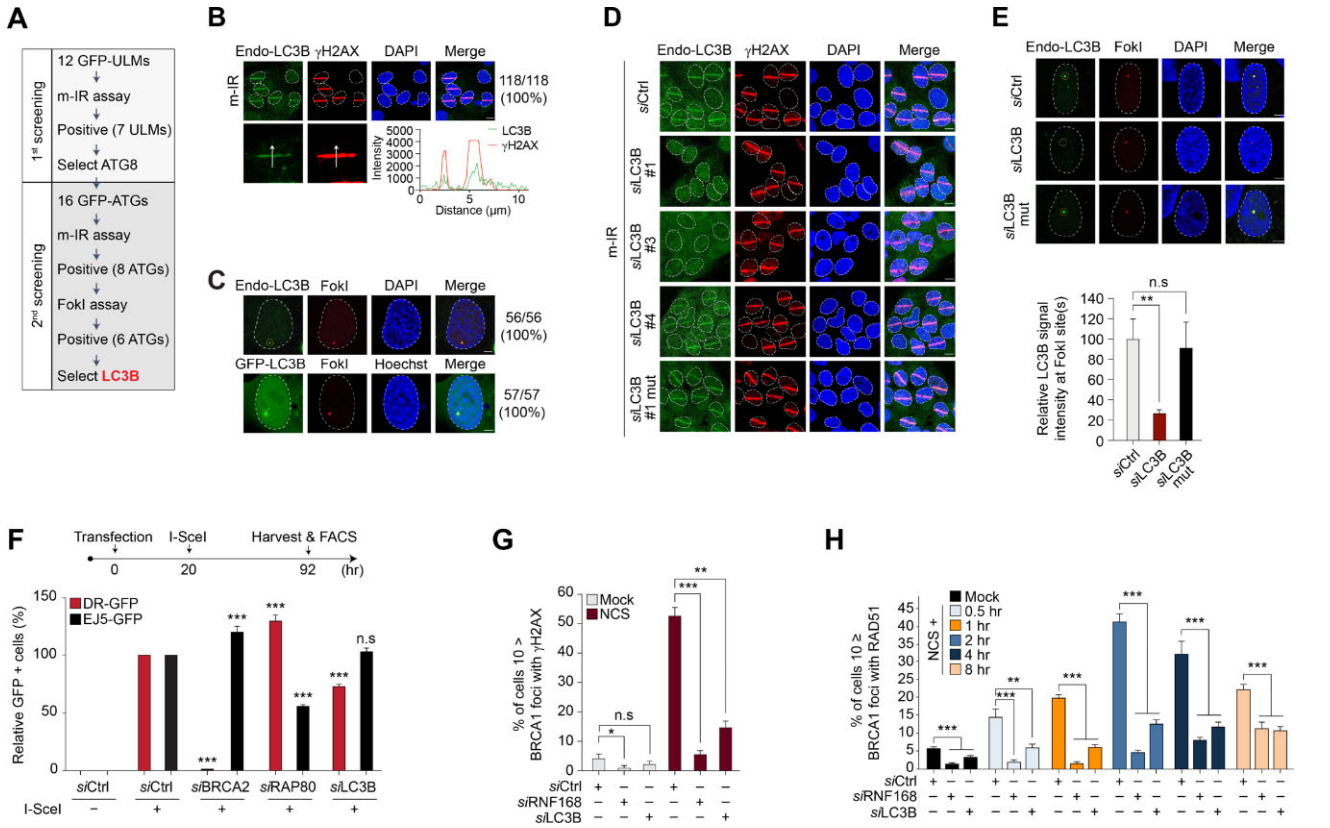

Figure 1. Identification of LC3B as an HR regulator. (**A**) An overview of the discovery of DDR-associated ULMs. (**B**) Co-localization of endogenous LC3B (endo-LC3B) with γH2AX at DNA damage sites in the m-IR system. Upper panel: visual representation. Lower panel: specific regions of interest, marked with white arrows, demonstrate signal intensity. (**C**) DSB-specific movement patterns of endo-LC3B and GFP-LC3B in the FokI system. (**D**) Validation of the migration and accumulation of endo-LC3B at m-IR-induced DSB sites using indicated *si*RNAs. (**E**) Verification of the movement of endo-LC3B to DSBs provoked by FokI, employing specified *si*RNA sets. The upper panel displays results, while the lower panel offers quantification. (**F**) Analysis of the effects of LC3B depletion on HR, highlighting its resemblance to the outcomes of *BRCA2* knockdown. Based on n = 6 independent experiments. (**G** and **H**), Examination of BRCA1 and RAD51 foci formation during HR following neocarzinostatin (NCS) treatment, considering LC3B reduction. For (**G**), from left to right: $n = 301, 308, 300, 305, 311$, and 304. For (**H**), from left to right: n values are 311, 331, 344, 313, 325, 354, 325, 325, 305, 314, 337, 300, 377, 388, 438, 346, 381 and 422. Statistical evaluations employed Tukey's multiple comparisons test. Levels of significance: *, $P < 0.05$; **, $P < 0.01$; ***, $P < 0.001$; n.s., non-significant. Data are presented as mean ± s.e.m. All scale bars represent 5 μm.

were treated with inhibitors such as PARP (PJ34, Olaparib), ATM (KU55933), ATR (VE-821), and DNA-PK (NU-7026) to decipher the pathways influencing LC3B's dynamics. Our data indicated a modest, though not statistically significant, reduction in LC3B's migration towards DSB sites induced by FokI upon ATM or PARP1 inhibition. Other inhibitors targeting pathways such as ATR and DNA-PK did not exhibit a substantial effect (Figure 2A and B). To more precisely define the roles of ATM and PARP1, we opted for siRNA-mediated knockdown experiments in place of an inhibitor-based method. As shown Figure 2C and D, we observed a significant decrease in GFP-LC3B signaling at these sites after siRNA-mediated knockdown of ATM, suggesting a key role for ATM in this process. However, PARP1 knockdown did not yield a significant change in LC3B recruitment compared to the control. This contrast underscores ATM's unique contribution to the DNA damage response involving LC3B, independent of PARP1 activity. Overall, these findings emphasize the specific importance of ATM in LC3B recruitment to DSB sites, in contrast to the broader and less significant impacts observed with the inhibition of PARP1, ATR and DNA-PK in this process.

Moreover, in evaluating autophagy's potential influence on LC3B's relocation to DSBs, consistent LC3B migration was noted even post-treatment with autophagy modulators (Figure 2E and F). Similarly, the transient depletion of ATG4B or p62, both integral to autophagy (34,35), did not alter LC3B's alignment with DSBs, implying that LC3B functions distinctively from autophagy flux (Figure 2G and H).

In our effort to delineate the functional domain guiding LC3B movement to FokI-induced DSBs, we fashioned a panel of LC3B mutants. Our 48−55 deletion mutant, which impairs the beta-2 sheet structure that facilitates interaction with LC3-interacting motifs (LIMs), was produced for its impacts on acetylation, p62 binding, and phosphorylation. The FLV/AAA and F52A mutants were created as p62 binding mutants, while the R68A and R68−70A mutants were designed as ATG4B and RNA binding mutants (RBMs), respectively. To investigate lipidation's effect on LC3B, a G120A mutant was developed, and, for phosphorylation, a T50A mutant was fashioned (Figure 2I and J). After transfecting these LC3B mutants into U2OS cells using a protocol analogous to the experiment in Figure 1A, we discerned that the lack of LC3B's RNA and p62 binding domains hindered its migration to sites of genomic damage (Figure 2K and L). Given prior experiments where p62 knockdown did not markedly influence LC3B's migration, this accentuates the distinct role of LC3B's RNA-recognition motif (RRM) in its relocation dynamics.

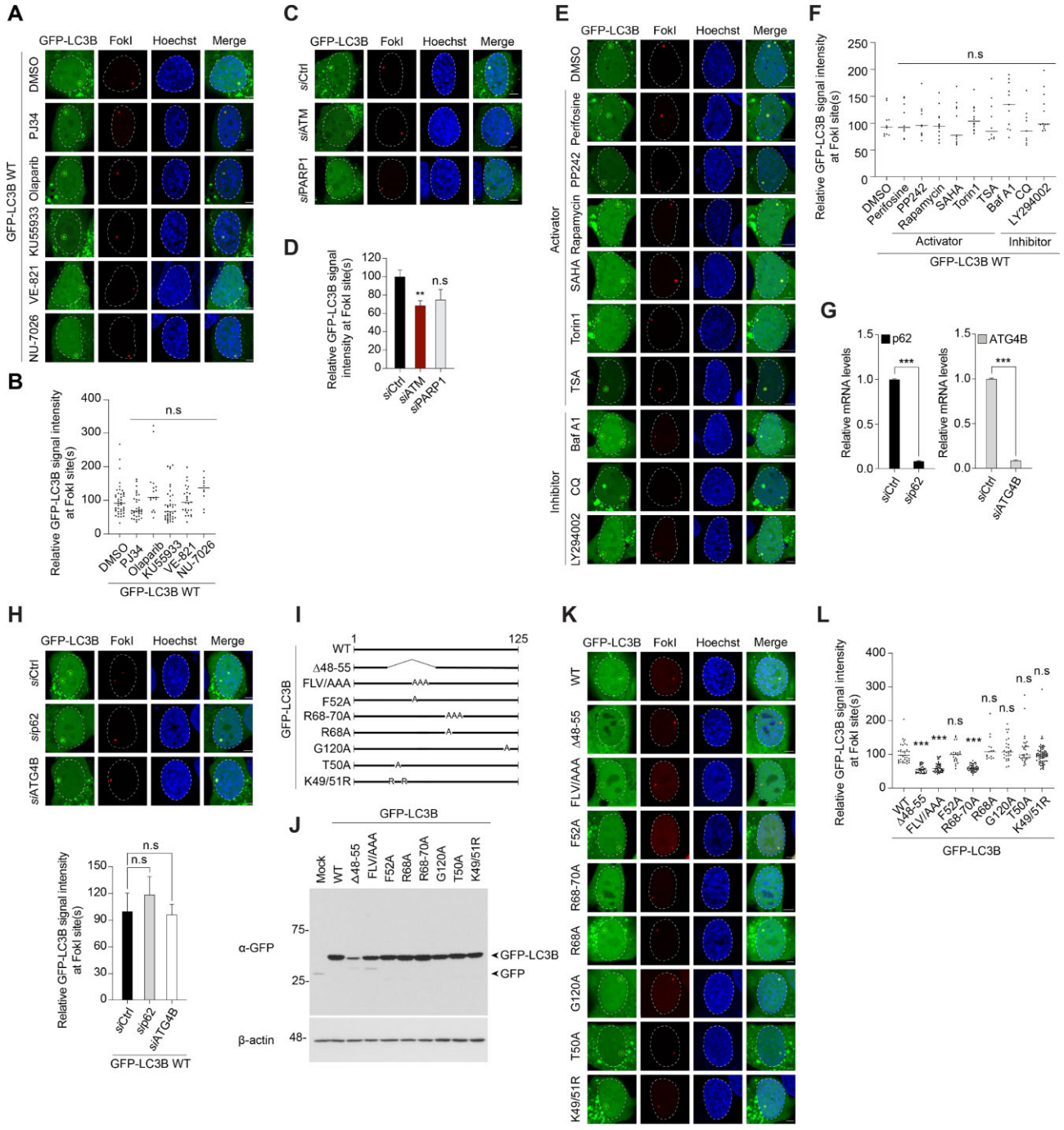

Figure 2. LC3B moves to DSBs via its RRM in an autophagy-independent manner. (**A**) Investigation of LC3B dynamics post administration of inhibitors targeting DDR's primary regulators. (**B**) Quantitative information corresponding to (A). From left to right: $n = 41$, 34, 17, 42, 26 and 10. (**C**) Recruitment of GFP-LC3B to DSBs in FokI cells transfected with indicated *si*RNAs. (**D**) Quantitative information corresponding to (**C**). *si*Ctrl: $n = 46$; *si*LC3B: $n = 32$; *si*LC3B mut: $n = 10$. (**E**) Accumulation of LC3B at FokI-induced DSBs subsequent to treatment with autophagy modulators. (**F**) Quantitative information corresponding to (E). From left to right: $n = 10$, 10, 12, 13, 11, 12, 10, 11, 9 and 13. (**G**) Quantitative RT-PCR assessment of mRNA expression in the cells transfected with the specified *si*RNAs. Based on $n = 3$ independent experiments. (**H**) Top: illustration of LC3B recruitment in FokI cells. Bottom: quantitative portrayal. *si*Ctrl: $n = 8$; *si*p62: $n = 10$; *si*ATG4B: $n = 14$. (**I**) Diagram depicting engineered LC3B mutants to discern functional domains influencing its trajectory to DSBs. (**J**) Western blot analysis displaying the expression levels of GFP-tagged LC3B WT and its mutants. (**K**) Illustrative images of GFP-LC3B mutant recruitment at FokI-induced DSBs. (**L**) Identification of distinct LC3B domains essential for its movement towards genomic damage locations. From left to right: n = 37, 37, 47, 23, 45, 15, 27, 34 and 74. Statistical evaluations employed Tukey's multiple comparisons test. Levels of significance: *, $P < 0.05$; **, $P < 0.01$; ***, $P < 0.001$; n.s, non-significant. Data are presented as mean ± s.e.m. All scale bars represent 5 μm.

In summary, these outcomes spotlight LC3B's inherent function in DDR. We illustrated that LC3B is intimately connected with DNA lesion dynamics, notably within the HR DNA repair pathway. The ATM pathway, contrary to PARP1, plays a significant role in directing LC3B to DSB sites as an upstream regulator. LC3B's relocation to DSBs is notably influenced by the ATM pathway, while it remains largely independent of other traditional upstream signaling pathways, including those involved in NHEJ. Crucially, specific LC3B domains, especially its RRM, are paramount for its migration to damaged chromatin, particularly DSBs. These revelations clarify LC3B's unique position in DDR, distinct from its role in autophagy.

LC3B directly binds to R-loops at DNA lesions and acts as a key player in TA-HRR

To elucidate the central role of LC3B's RRM in the HRR process, endo-LC3B was initially depleted (Figure 3A). Following this, we reintroduced either LC3B-wild type, -RBM or -FLV/AAA variants and subsequently assessed their influence on HR efficiency via the DR-GFP reporter system (Figure 3A). Notably, only the wild-type LC3B was able to fully restore HR functionality, underscoring the key role for LC3B's RRM in the HR pathway.

Subsequently, to discern the RNA dependency of LC3B's DSB recruitment, we first probed whether RNAs were present at FokI sites, as previously described by Alyshia Newhart *et al.* (36) We observed that mCherry-FokI colocalized with the S9.6 antibody, indicating a pronounced accumulation of RNAs at FokI sites. Furthermore, we confirmed that RNase H1 could displace these RNAs from FokI sites (Supplementary Figure S3A). This suggests that these RNAs might be DNA/RNA hybrids, like R-loops, generated by DNA damage near transcriptionally active regions. In light of this, we exposed FokI cells to either RNase A or RNase H and then monitored LC3B recruitment (Figure 3B, left panel). Interestingly, while LC3B's DSB recruitment was unaffected by RNase A treatment, it was markedly diminished following RNase H treatment, hinting at a substantial interplay between LC3B and DNA/RNA hybrids during DSB repair (Figure 3B, left panel). To further probe this interaction, we employed the S9.6 antibody and EGFP-tagged hybrid binding domain (HBD) of RNase H. This approach highlighted a notable accumulation of both markers at FokI-induced DSB sites (Figure 3B, right panel). This observation provides further support for the presence of R-loops at these locations and strengthens the hypothesis that LC3B's recruitment to DSBs is facilitated by its interaction with DNA/RNA hybrids.

Recognizing the established presence of R-loops at DNA damage sites, we explored potential interactions between LC3B and R-loops using the S9.6 antibody. Notably, depleting LC3B resulted in a marked uptick in R-loop accumulation at the FokI site, even surpassing levels observed when XPG, a known factor in TA-HRR-linked R-loop resolution, was depleted (Figure 3C). These observations accentuate the critical role of LC3B in R-loop resolution, and, by extension, its possible involvement in associated DNA repair mechanisms, either directly or indirectly.

In this context, and aiming to further understand the intricate relationship between LC3B and mechanisms of HRR, the DR-GFP reporter assay was implemented to ascertain the roles of R-loops in HRR. RNase H treatment, which is known to dismantle R-loops, significantly diminished the proportion of GFP-positive cells ($P < 0.01$), indicating that intact R-loops may be conducive to HRR. Conversely, LC3B knockdown, implicated in the accumulation of R-loops, led to a comparable decrease in HR efficiency, suggesting that LC3B plays a role in the resolution of R-loops, thus promoting HR. Notably, the additional suppression of LC3B in RNase H overexpressed cells did not exacerbate the HR defect, implying that LC3B's function in HR is contingent upon the presence of R-loops. The absence of an additive effect when both RNase H and LC3B are modulated indicates an epistatic relationship, with LC3B's role in HR repair likely being mediated through regulation of R-loop dynamics (Supplementary Figure S3B).

Expanding upon this understanding, resolution of R-loops by LC3B was further confirmed by dot blotting of genomic DNA from non-damaged cells or damaged cells with LC3B knockdown. Our findings indicate that the increase in R-loops is not merely confined to sites of DNA breaks but extends globally across the genome in cells depleted of LC3B (Supplementary Figure S3C). This observation suggests that LC3B plays a role in managing R-loop levels not only at DNA break sites but throughout the cell. The global elevation of R-loops in LC3B-depleted cells underscores the importance of LC3B in maintaining genomic integrity and preventing R-loop accumulation, which can lead to genomic instability and DNA damage.

To strengthen our conclusions, FokI cells were treated with 5,6-dichlorobenzimidazole 1-β-D-ribofuranoside (DRB), a recognized inhibitor of RNA PolII that targets the positive transcription elongation factor b (P-TEFb) (37). We subsequently gauged its impact on R-loop formation. As expected, DRB-treated cells manifested neither signs of nascent RNAs in whole cells nor R-loop accumulation at the FokI site (Supplementary Figure S3D and E). Pursuing this, we evaluated the spatial distribution of endo-LC3B at FokI sites during DRB treatment. Aligned with our expectations, post-DRB treatment, the recruitment of LC3B towards DSBs was significantly reduced. However, upon DRB removal, LC3B swiftly relocated to the DSBs (Figure 3D). A congruent pattern emerged with flavopiridol treatment, which mirrors DRB's activity (Supplementary Figure S3F) (38). These observations emphasize the likely R-loop dependency in LC3B's trajectory to FokI sites.

Seeking a deeper understanding of the relationship between LC3B and R-loops, we executed an *in vitro* R-loop binding assay via electrophoretic mobility shift assay (EMSA), deploying equivalent amounts of recombinant LC3B WT and its RBM (Figure 3E). Strikingly, recombinant LC3B WT displayed direct binding capabilities to not only R-loops but also various DNA/RNA hybrids (Figure 3F). In contrast, LC3B-RBM failed to bind to R-loops or other DNA/RNA hybrids (Figure 3G and H). To discern the specificity of LC3B's binding to RNA, DNA, or hybrids, recombinant LC3B WT was introduced into the EMSA in tandem with ds-DNA, ssDNA, or dsRNA probes. LC3B exhibited no binding to any of these probes (Figure 3I). To further strengthen our data suggesting interactions between LC3B and R-loops, the hybrid binding domain (HBD) of RNase H was purified (Supplementary Figure S3G). This HBD was used for EMSA experiment instead of S9.6 antibody. As we expected, HBD strongly bound to R-loops and hybrids rather than to the other probes, supporting LC3B's specific interactions with these targets (Supplementary Figure S3H and I). This

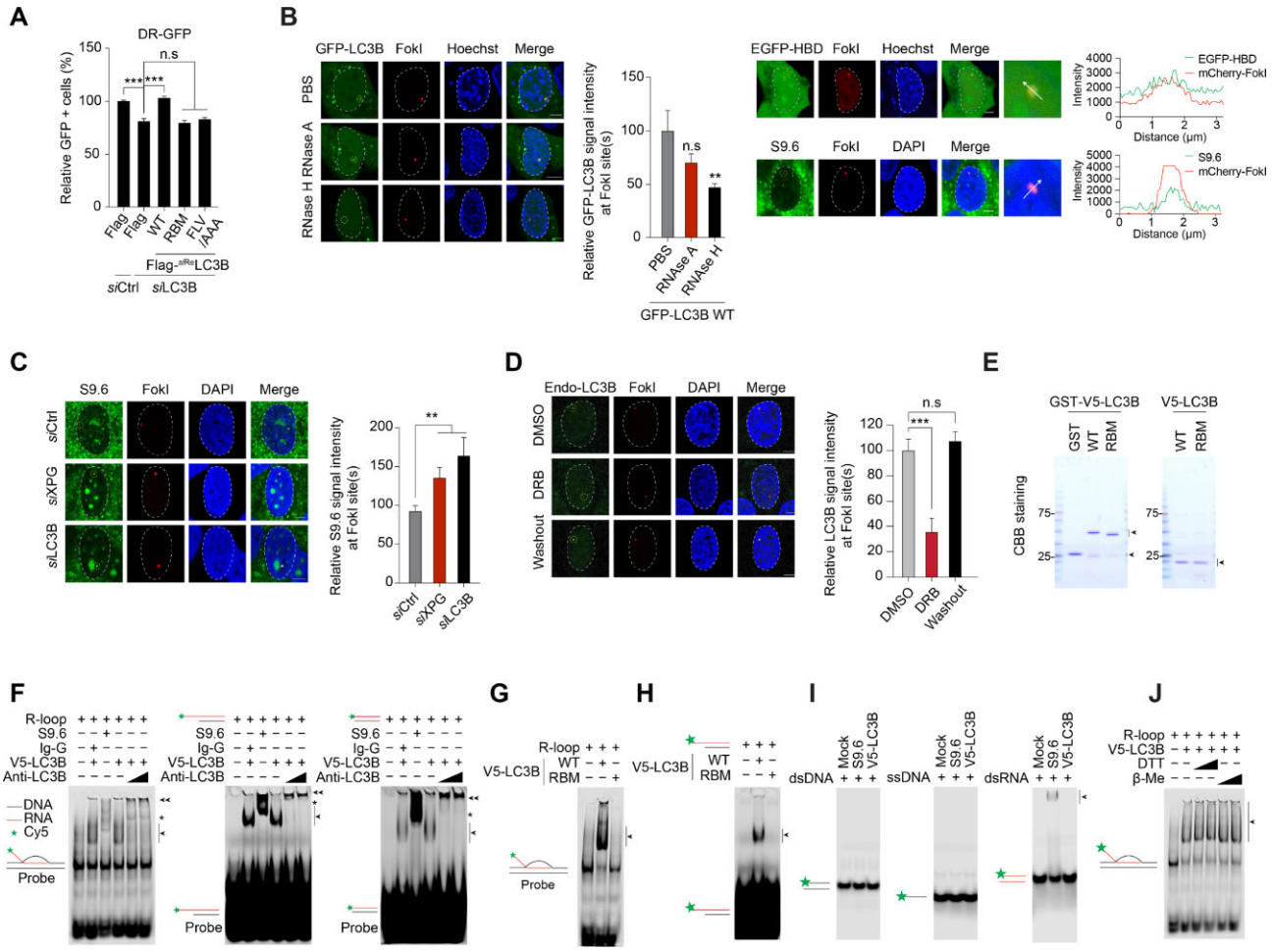

Figure 3. LC3B directly binds to DNA/RNA hybrids including R-loops. (**A**) Evaluation of HR efficiency following reintroduction of LC3B variants in endo-LC3B depleted cells using the DR-GFP reporter system. Based on $n = 6$ independent experiments. (**B**) Left: Representative images and quantificaiton of LC3B to DSBs post-treatment with RNase A or RNase H in FokI cells. PBS: $n = 10$; RNase A: $n = 11$; RNase H: $n = 13$. Right: Recruitment of EGFP-HBD (Top) and accumulation of R-loops (bottom) at DSBs induced by FokI. Left panel: visual representation. Right panel: specific regions of interest, marked with white arrows, demonstrate signal intensity. (**C**) Left: Increased R-loop accumulation at the FokI site following depletion of LC3B or XPG. Right: Associated quantification. *si*Ctrl: $n = 9$; *si*XPG: $n = 8$; *si*LC3B: $n = 8$. (**D**) Left: Dynamics of endo-LC3B relocation to DSBs after DRB treatment in FokI cells. Right: Quantitative evaluation. DMSO: $n = 7$; DRB: $n = 7$; DRB + Washout: $n = 7$. (**E**) Purified recombinants analyzed using SDS–PAGE gel, stained with Coomassie blue. Left: GST (alone), GST-V5 LC3B WT, and RBM. Right: V5-LC3B WT and RBM. (**F**) Direct *in vitro* association of LC3B with DNA/RNA hybrids demonstrated through an R-loop binding assay. (G and H) Altered interaction between LC3B and R-loops (**G**) or DNA/RNA hybrids (**H**) due to mutated RNA-binding motif. (**I**) Verification of LC3B's *in vitro* binding to dsDNA, ssDNA and dsRNA via EMSA. (**J**) Enhanced binding of LC3B to the R-loop after treatment with DTT or β-mercaptoethanol (β-Me). Statistical evaluations employed Tukey's multiple comparisons test. Levels of significance: *, $P < 0.05$; **, $P < 0.01$; ***, $P < 0.001$; n.s, non-significant. Data are presented as mean ± s.e.m. All scale bars represent 5 μm.

confirms that LC3B's localization to sites of genomic damage is predominantly orchestrated by its specific affinity with R-loops.

While our data showcased an interaction between LC3B and DNA/RNA, it was essential to address whether this binding might be influenced by contaminants co-purified with the recombinant LC3B protein—particularly proteins with RNA-binding capabilities. It is noteworthy that LC3B protein lacks cysteine residues, ensuring it does not establish disulfide bonds in its tertiary structure. Conversely, a majority of RNA-binding proteins, inclusive of RNases, derive their tertiary formations via disulfide bonds. Leveraging this distinction, we executed the EMSA assay in the presence of DTT and β-mercaptoethanol (β-ME), agents that reduce disulfide bonds between cysteines (39). Notably, even under these conditions, LC3B maintained its affinity to DNA/RNA hybrids (Figure 3J). This firmly dispels the notion that RNA-linked proteins, especially those predicated on cysteine, could have influenced our preliminary findings.

R-loops play a pivotal role in DDR, especially in transcriptionally active regions. Although aberrant accumulation of R-loops can be deleterious, they are indispensable for transcription-associated DNA repair processes (40–44). To elucidate the biological interplay between R-loops and LC3B at DSBs, we utilized the DIvA system, pioneered by the Legube group. This robust system enables the generation of DSBs at specific genomic locations across various chromatin contexts, encompassing both transcriptionally active and inactive regions (25). A standout feature of the DIvA system is its several transcriptionally active genes (such as *CCDC47*, *PIP5KL1*, *ANP32A* and *LYRM2*) and inactive genes (like *RXRA* and *UBE2G1*) that are well characterized as specific gene tar-

gets of AsiSI, an endonuclease activated by treatment with 4-hydroxytamoxifen (4-OHT) (9,10).

Utilizing the DIvA system, we monitored LC3B's recruitment to the proximal region of AsiSI-targeted sites in both transcriptionally active and inactive genes using Chromatin immunoprecipitation (ChIP) analysis. Notably, we observed that LC3B predominantly localized to transcriptionally active regions in conjunction with polymerase II, while it mostly avoided inactive sites in 4-OHT-treated DIvA cells (Figure 4A). Building on this observation, we performed a similar experiment in the presence or absence of DRB. We found that LC3B's recruitment to the transcriptionally active regions with DNA breaks diminished significantly with DRB treatment, with no similar effect on transcriptionally inactive genes (Figure 4B).

To confirm R-loop accumulation in these transcriptionally active regions, DIvA cells were treated with either mock or RNase H after 4-OHT induction. A subsequent DNA/RNA-immunoprecipitation (DRIP) assay using the S9.6 antibody verified R-loop enrichment in these active regions (Figure 4C and Supplementary Figure S3J). In the same experimental settings, our monitoring of LC3B recruitment revealed a noticeable reduction in LC3B's presence following RNase H treatment. Intriguingly, this intervention did not impact PolII recruitment, suggesting that R-loops primarily drive LC3B recruitment dynamics (Figure 4D). Moreover, with the auxin-inducible degron (AID)-DIvA system, we gathered compelling evidence that LC3B recruitment and γH2AX levels were reduced after indole-3-acetic acid (IAA) treatment, which promotes AID degradation and consequently inhibits AsiSI activity (Figure 4E and Supplementary Figure S3K). These results underscore the importance of active transcription and R-loops in guiding LC3B recruitment during the transcription-coupled DNA damage response.

Recently, there has been a surge in research focused on DNA repair processes associated with transcription, such as TA-HRR and TA-EJ (9,10). Several key regulatory proteins related to these processes have been identified. Based on our findings, LC3B seems more intricately associated with TA-HRR than with TA-EJ. This perspective prompted us to investigate the relationship between LC3B and primary TA-HRR regulators. In experiments using the DR cell line, we assessed HR defects resulting from knockdowns of central TA-HRR regulators like RAD52, XPG, and BRCA1, comparing them to defects observed post LC3B knockdown. Our results indicated comparable HR defect levels under both knockdown conditions, hinting at a close association between LC3B and TA-HRR (Figure 4F). Additionally, our study extended to an examination of double siRNA treatments, specifically XPG-LC3B and RAD52-LC3B knockdowns. Notably, the simultaneous depletion of XPG and LC3B, as well as RAD52 and LC3B, did not show a significant additive effect on the percentage of GFP-positive cells with defects compared to that following the depletion of LC3B alone (Figure 4G). This suggests a collaborative function of LC3B with these TA-HRR mediators, rather than a layered contribution to the mechanism. Hence, LC3B's influence on TA-HRR appears to be a critical facet of a shared pathway with established TA-HRR components, rather than a mere additive factor.

In an attempt to characterize the association between LC3B and the TA-HRR pathway, we observed the dynamics of RPA32 and BRCA1 foci, intrinsic markers of the TA-HRR pathway, after DRB treatment and LC3B knockdown in the context of NCS exposure. Remarkably, the decrease in the number of these foci after DRB treatment mirrored the reduction seen with LC3B knockdown (Figure 4H and Supplementary Figure S3L). Fascinatingly, when combining DRB treatment with LC3B depletion, we did not observe an exacerbation of the individual effects, which would indicate an effect that is epistatic. These findings strongly suggest that LC3B operates within the same biological pathway or functional hub as these essential TA-HRR components, highlighting its critical role in the molecular dynamics of TA-HRR.

LC3B regulates *BRCA1* mRNA stability through direct interactions with 3′UTR AREs

As illustrated in Figure 4H, LC3B knockdown led to a pronounced reduction in BRCA1 foci. These findings position LC3B as a pivotal actor in the recruitment of BRCA1 to DSBs during TA-HRR, potentially via an R-loop-dependent mechanism. Probing deeper into the relationship between LC3B and BRCA1 recruitment to DSBs, we examined the mRNA and protein levels of BRCA1 post LC3B knockdown. Notably, we identified a 60% decline in BRCA1 protein levels and 30% reduction in its mRNA expression (Figure 5A and B). These insights emphasize LC3B's significant impact on the mRNA stability of *BRCA1*, possibly independent of its role at DSBs.

Recent studies from multiple research groups have highlighted LC3B's role in regulating mRNA stability by interacting with AU-rich elements in the UTR regions through its RRM. Expanding on this knowledge, we pinpointed two distinct AU-rich elements (AREs) in the 3′UTR of BRCA1, specifically designated as ARE1 and ARE2. These elements are precisely located at positions +5954 ∼ +5973 and +5988 ∼ +6004, as illustrated in Supplementary Figure S4A. Interestingly, ARE2 encompasses binding sites for the HuR protein (45). This raises the intriguing possibility that LC3B may directly interact with the 3′UTR region of BRCA1.

To substantiate this, we synthesized biotin-labeled RNA probes: two (#1 and #2) targeting distinct AREs, and a third (#3) encompassing both AREs, with all probes approximately 150 bases in length (Supplementary Figure S4A and Supplementary Table S5). Simultaneously, we checked the quantity and quality of the probes using a dot blot as indicated (Supplementary Figure S4B). Aligning with our hypothesis, endo-LC3B was pulled down with all RNA probes, akin to HuR, while the poly(A) control displayed no such interaction. Interestingly, endo-LC3B exhibited a slight preference for probe #1 over #2; in contrast, HuR leaned towards #2 (Figure 5C). This suggests distinct binding affinities for the AREs present in *BRCA1*'s 3′UTR.

Concurrently, another RNA pull-down assay was carried out using recombinant GST-V5-LC3B WT, -RBM, or GST in similar molar ratios instead of cell lysates. As anticipated, only GST-V5-LC3B WT displayed binding to probes #1 and #3, showing a stronger affinity for #1 (Figure 5D). Neither GST nor GST-V5-LC3B RBM exhibited any probe binding. While LC3B WT had a minor interaction with the poly(A) probe, our results robustly suggest that LC3B leverages its RRM in a manner aligned with its binding to DNA/RNA hybrids when engaging with the ARE(s) in *BRCA1*'s 3′UTR.

To confirm that the observed interactions indeed occur intracellularly, we executed native RNA immunoprecipitation (nRIP) paired with high-throughput sequencing (nRIP-seq). This approach facilitates the identification of enduring inter-

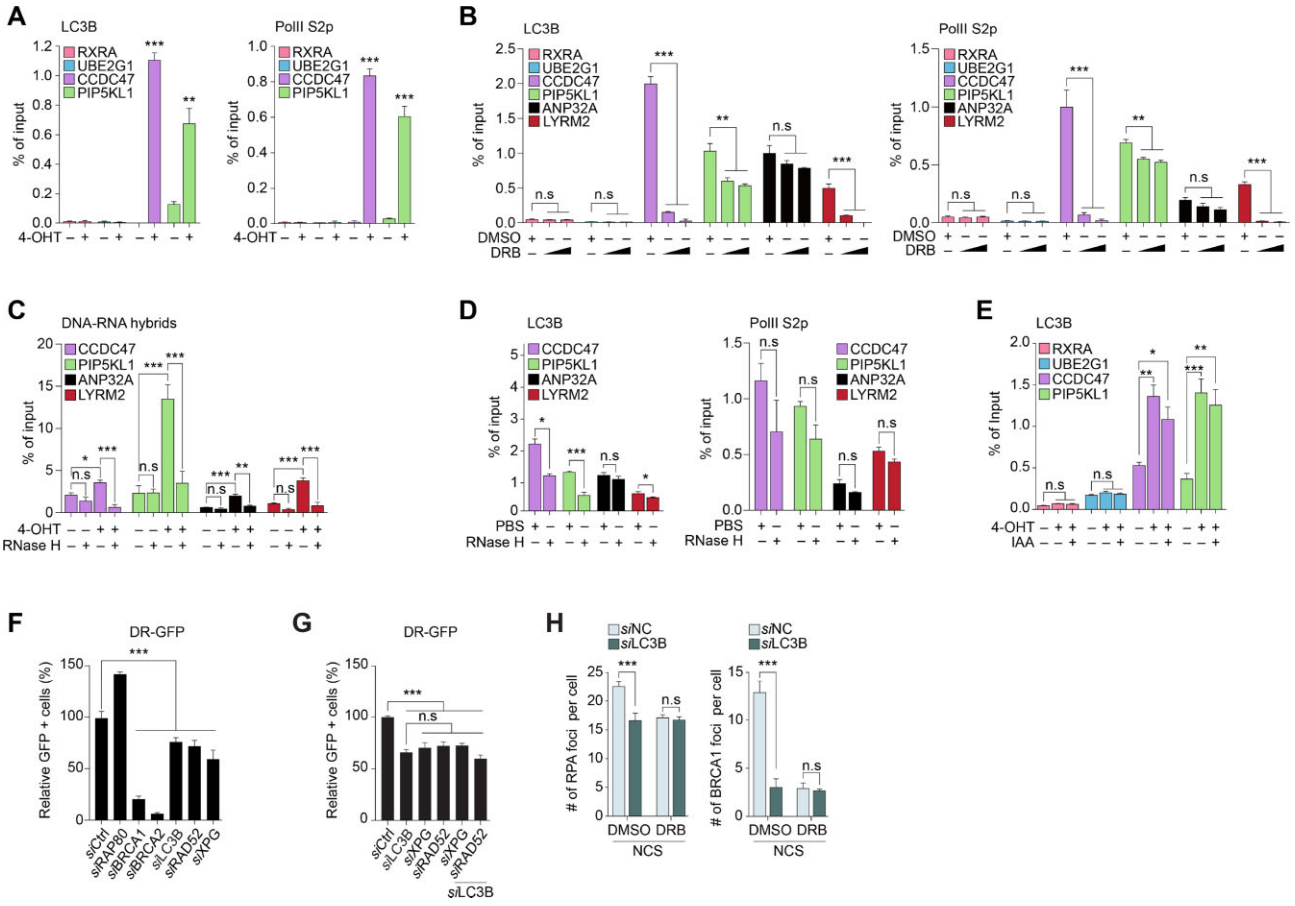

Figure 4. LC3B facilitates R-loop-mediated TA-HRR. (**A**) ChIP analysis showcasing LC3B (left) and PolII S2p (right) recruitment to DSB-induced transcriptionally active and inactive genes in DIvA. (**B**) Patterns of LC3B (left) and PolII S2p (right) recruitment with or without DRB at transcriptionally dynamic genes in DIvA. (**C**) DRIP analysis indicating DNA/RNA hybrids with or without RNase H at transcriptionally active genes in DIvA. (**D**) ChIP results emphasizing the RNase H effect on LC3B (left) and PolII S2p (right) recruitment to transcriptionally active regions in DIvA. (**E**) AID-DIvA-based monitoring of LC3B recruitment following IAA administration. (**F**) HR defects mirroring parallels between knockdowns of TA-HRR primary regulators and LC3B in DR cells. Based on $n = 6$ independent experiments. (**G**) Analysis of the effect of simultaneous knockdown of the TA-HRR primary regulator and LC3B using the DR-GFP reporter system. Based on $n = 3$ experiments. (**H**) Dynamics of RPA and BRCA1 foci post-application of DRB or depletion of LC3B under NCS conditions. From left to right: n = 131, 191, 104, 199, 152, 133, 156 and 138. Statistical analyses for figures (A–G) utilized Tukey's multiple comparisons test, while figures (H) employed an unpaired *t*-test. Levels of significance: *, $P < 0.05$; **, $P < 0.01$; ***, $P < 0.001$; n.s, non-significant. Data are presented as mean ± s.e.m. All scale bars represent 5 μm.

actions between RNAs and cellular proteins using the LC3B antibody (Figure 5E).

Adhering to this methodology and upon procuring the nRIP-seq data, our primary objective was to discern whether the ARE(s) in *BRCA1*'s 3′UTR were efficiently pulled down by the LC3B antibody. As demonstrated in Figure 5E, there was significant enrichment of reads originating from *BRCA1*'s 3′UTR with the ARE(s), indicating these regions are favored native binding sites for endogenous LC3B.

To ensure the robustness of our sequencing data, we utilized FastQC for quality control. The sequencing reads were subsequently aligned to a reference genome using STAR v.2.7.1a, achieving a high mapping rate. After alignment, we quantified transcript abundance, and the TPM values displayed a broad spectrum of expression across different transcripts, reinforcing the quality of our dataset. Intriguingly, LC3B-associated reads were predominantly situated approximately 1000 base pairs from both the TSS and TES (Figure 5F). Applying a stringent threshold for peak calling, we identified 5285 significant peaks associated with LC3B. The coverage analysis revealed that the mean coverage for LC3B-associated peaks was 99%, signifying its comprehensive binding across the transcriptome (Figure 5G). In contrast, the IgG controls demonstrated minimal coverage, underscoring the specificity of the LC3B pull-down.

Furthermore, we noted a substantial enrichment of LC3B-associated peaks in the 3′UTR of target mRNAs (*P*-value < 0.01), implying a crucial role of LC3B-RNA interactions in modulating mRNA stability within cellular mechanisms (Figure 5H). Next, to discern conserved LC3B binding motifs to target mRNAs, we undertook motif analysis using RAST-peak-motif. Consequently, we identified 13 distinct conserved motifs, among which a specific pattern emerged (as detailed in Supplementary Table S10). This pattern correlates with previously recognized LC3B-binding traits, especially its affinity for AU-rich elements (Figure 5I). To further corroborate these observations, we selected the top 7 motifs for EMSA analysis (Supplementary Figure S4C and Supplementary Table S5). The EMSA outcomes affirmed that LC3B directly associates with 5 out of these 7 conserved motifs. Notably, LC3B manifested a pronounced binding inclination towards AU-rich conserved motifs, specifically #1, #2 and

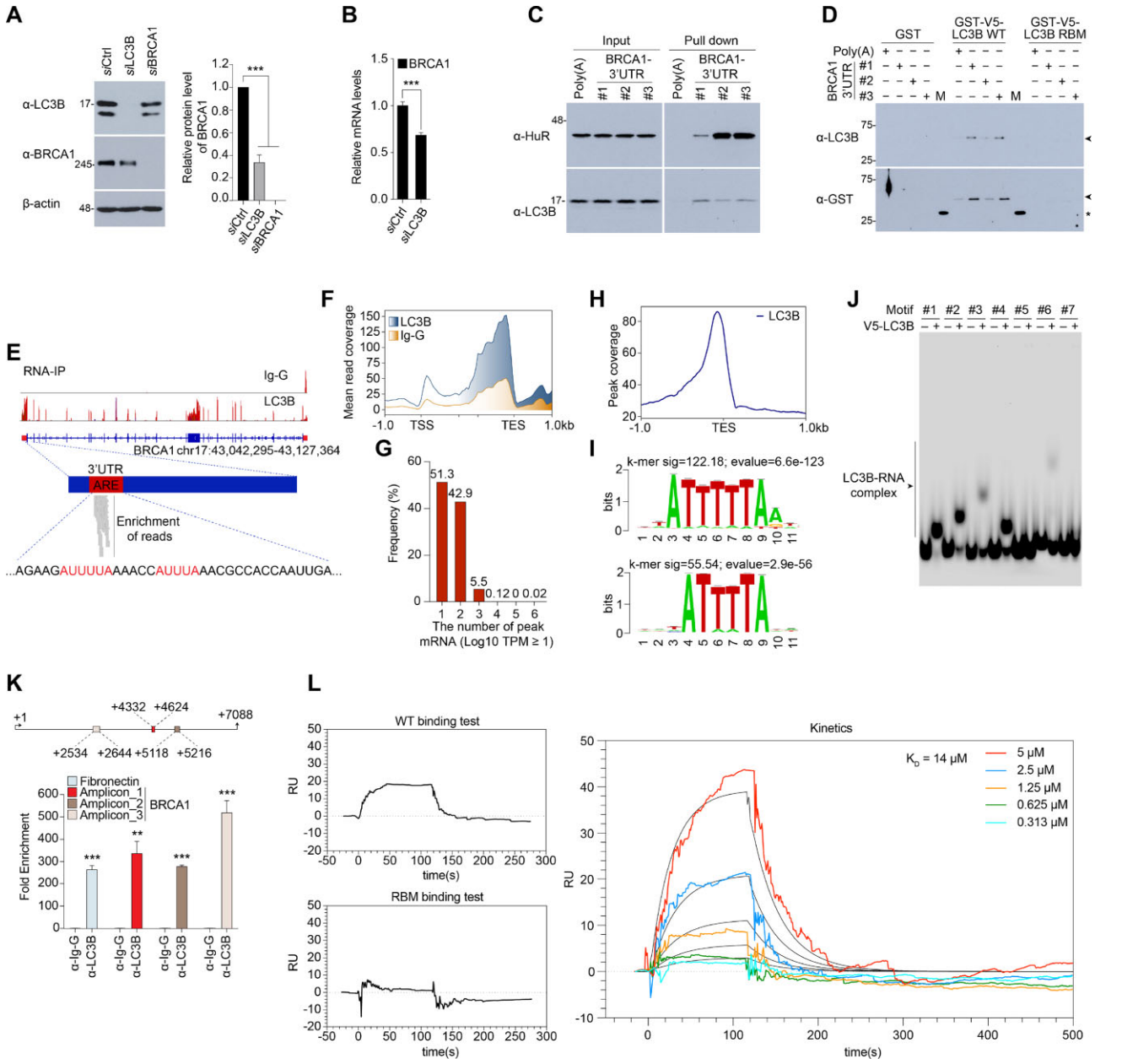

Figure 5. LC3B directly binds to AU-rich elements on BRCA1 3′UTR and regulates BRCA1 mRNA stability. (**A**) Western blot showcasing a 60% reduction in BRCA1 protein concentrations upon LC3B knockdown. (**B**) Quantitative RT-PCR results indicating a 30% reduction in *BRCA1* mRNA levels following LC3B knockdown. Based on $n = 3$ independent experiments. (**C**) RNA pull-down assay employing biotin-labeled RNA probes that correspond to the AREs within *BRCA1*'s 3′UTR. Distinct binding patterns of endo-LC3B and endo-HuR to these probes are depicted. (**D**) RNA pull-down involving recombinant GST-V5-LC3B variants reveals only GST-V5-LC3B WT has an affinity for the ARE probes. (**E**) nRIP-seq data highlighting significant enrichment within the 3′UTR region of *BRCA1* that contains AREs. (**F**) A distribution map of LC3B-associated reads localized around the TSS and TES domains. (**G**) Coverage analysis demonstrating extensive LC3B binding throughout the transcriptome. (**H**) A marked concentration of LC3B-associated peaks is observed within the 3′UTR of target mRNAs. (**I**) Motif evaluation unveils LC3B's preference for certain conserved patterns, particularly AU-rich elements. (**J**) EMSA assessment of LC3B interactions with the seven conserved motifs depicted in Supplementary Figure S4C. (**K**) Endogenous interaction between LC3B and *BRCA1*'s mRNA was confirmed by nRIP-qPCR with indicated amplicons. The *Fibronectin* mRNA was used as positive control and Ig-G was used as negative control for nRIP-qPCR. $n = 3$ independent experiments. (**L**) Surface Plasmon Resonance (SPR) analysis detailing the binding dynamics between LC3B and ARE(s) present in *BRCA1*'s 3′UTR. For panels (A) and (K), statistical evaluations were undertaken using Tukey's multiple comparisons test, whereas panel (B) employed an unpaired *t*-test. Levels of significance: *, $P < 0.05$; **, $P < 0.01$; ***, $P < 0.001$; n.s., non-significant. Data are presented as mean ± s.e.m.

#4 (Figure 5J). Among these, the conserved AUUUA sequence in the #1 motif matches the ARE sequences found at positions + 5962 ∼ 5966 and +6000 ∼ 6004 in the 3′UTR of BRCA1's mRNA. To further confirm the physiological interaction between LC3B and BRCA1 mRNA, we carried out native RNA immunoprecipitation using the LC3B antibody. This was followed by quantitative PCR (nRIP-qPCR) using the indicated amplicons—primers specifically designed to amplify *BRCA1* mRNA. Consistent with earlier findings related to LC3B's interaction with fibronectin mRNA, LC3B was found to bind with *BRCA1* mRNA. On the other hand, no binding was observed with Ig-G (Figure 5K).

These outcomes present persuasive evidence to support LC3B's specificity in discerning and binding to AU-rich elements on 3′UTRs of *BRCA1* mRNAs. Considering the established regulatory attributes of these AU-rich elements in mRNA turnover and stability, it is conceivable that LC3B functions as a pivotal regulator in these pathways.

In summary, the binding kinetics between LC3B and ARE(s) in *BRCA1*'s 3′UTR were analyzed via SPR utilizing an iM-SPR_ProX instrument (iCLUEBIO, Republic of Korea). As anticipated, LC3B-RBM exhibited no binding affinity to the ARE(s) in *BRCA1*'s 3′UTR (Figure 5L). In contrast, LC3B WT demonstrated formidable binding, with a KDvalue of 14 μM (Figure 5L).

These data prompted us to ask the following question: is LC3B's regulation of TA-HRR solely mediated by modulation of BRCA1 expression, or is regulation of R-loops also required? To address this, we specifically introduced the coding sequence (CDS) of BRCA1 into LC3B-depleted cells. This strategy was employed to ascertain whether BRCA1 CDS alone could rectify the HR deficiency induced by LC3B knockdown. The data, as presented in Supplementary Figure S4D and E, showed that ectopic expression of BRCA1 CDS positively influenced HR repair efficiency. Nonetheless, the level of HR repair did not fully recover to that of the control siRNA-treated cells. This observation suggests that, while BRCA1 is a significant factor in HR repair, the role of LC3B is not limited to the modulation of BRCA1 expression. Direct interaction between LC3B and R-loops appears to be critical to LC3B's regulation of the TA-HRR pathway. These findings highlight the complex relationship between LC3B, BRCA1, and R-loop dynamics, indicating that the influence of LC3B on TA-HRR involves a network of interactions that extends beyond a singular pathway.

Taken together, our findings present a broader perspective, indicating that LC3B not only regulates the stability of BRCA1 mRNA but also plays a vital role in modulating R-loop dynamics during TA-HRR. This dual functionality underscores the critical significance of LC3B in the TA-HRR process.

LC3B promotes chromosomal stability through TA-HRR guidance

Subsequently, we observed 53BP1 foci formation, which is involved in the choice of NHEJ and HRR pathways, under LC3B depletion conditions. Intriguingly, the number of 53BP1 foci did not increase, even when there was a significant decrease in the BRCA1 foci number. Typically, cells with a defect in HR exhibit a high number of 53BP1 foci; however, this phenomenon was not apparent in our experiments. A closer inspection of our primary data revealed no discernible change in the number of 53BP1 foci (Figure 6A). Yet, there was a noticeable reduction in their size (Supplementary Figure S5A).

We postulated that this observation might stem from continuous DSBs triggered by 4-OHT. In follow-up experiments, we applied IAA to AID-DIvA cells to inhibit persistent DNA breaks and subsequently assessed the number of 53BP1 foci. Predictably, we verified that 53BP1 foci formation was spurred by LC3B knockdown. This indirectly suggests that when TA-HRR is defective due to LC3 depletion, the cell encourages a transition to NHEJ in collaboration with 53BP1 (Figure 6B and Supplementary Figure S5B).

For a direct examination of TA-HRR defects during LC3B knockdown, we conducted an end-resection assay, which evaluates an essential HR step. Initially, the assay's accuracy was affirmed by a decrease after DRB treatment, with no alterations observed upon administering NU7026, a DNA-PK inhibitor (Figure 6C, left panel). Upon LC3B depletion, we noted an end-resection defect akin to that observed in BRCA1 and MRE11 depletion, underscoring LC3B's fundamental role in end-resection during TA-HRR. Notably, transfection with si53BP1 and non-targeting siLC3B mut resulted in the absence of this end-resection defect, further emphasizing LC3B's essential role in BRCA1-mediated TA-HRR (Figure 6C, right panel).

To delve deeper into the biological implications of an LC3B defect, we evaluated sister chromatid exchange (SCE) and interchromatid fusion (ICF) post LC3B knockdown. As anticipated, SCE frequency diminished with LC3B knockdown (Figure 6D), while ICF frequency increased (Figure 6E). These alterations mirrored those observed during the depletion of control factors RAD52 and Lig4. In our concluding observations, reintroducing LC3B WT appeared to offset the effects initiated by LC3B depletion; conversely, LC3B-RBM failed to do so (Figure 6F and G and Supplementary Figure S5C and D). Moreover, while LC3B WT knockdown manifested significant effects, knockdowns of p62 and ATG4B remained inconspicuous (Figure 6H and I and Supplementary Figure S5E and F).

Collectively, our results present initial evidence that LC3B, a major autophagy regulator, directly influences the maintenance of chromosomal stability via TA-HRR, independent of autophagy, amidst genomic damage.

Discussion

The intricate landscape of DDR comprises various pathways and molecules that collectively protect genomic integrity. In this realm, we delve into the relationship between LC3B and DDR, broadening our understanding of autophagy beyond its conventional roles.

Our results underscore LC3B's direct engagement, mediated by its RRM, with R-loops in transcriptionally active DNA areas. While LC3B's RNA-binding capability is well-established, our investigation reveals a novel interaction between LC3B and RNA/DNA hybrids. Intrigued, we consulted public structural data on LC3B and observed a striking structural resemblance between *E. coli* RNase H1 and LC3B. Specifically, the RRR and FLV domains of LC3B closely mirror the structure of RNase H1 (Supplementary Figure S6). While this parallelism is noteworthy, it does not elucidate LC3B's dual affinity for single-stranded RNA and DNA/RNA hybrids. Nonetheless, it lays a foundational insight into LC3B's potential interaction with these hybrids.

Interestingly, Figure 3I indicates LC3B's discernment, showing no affinity for ssDNA, dsDNA or dsRNA, which

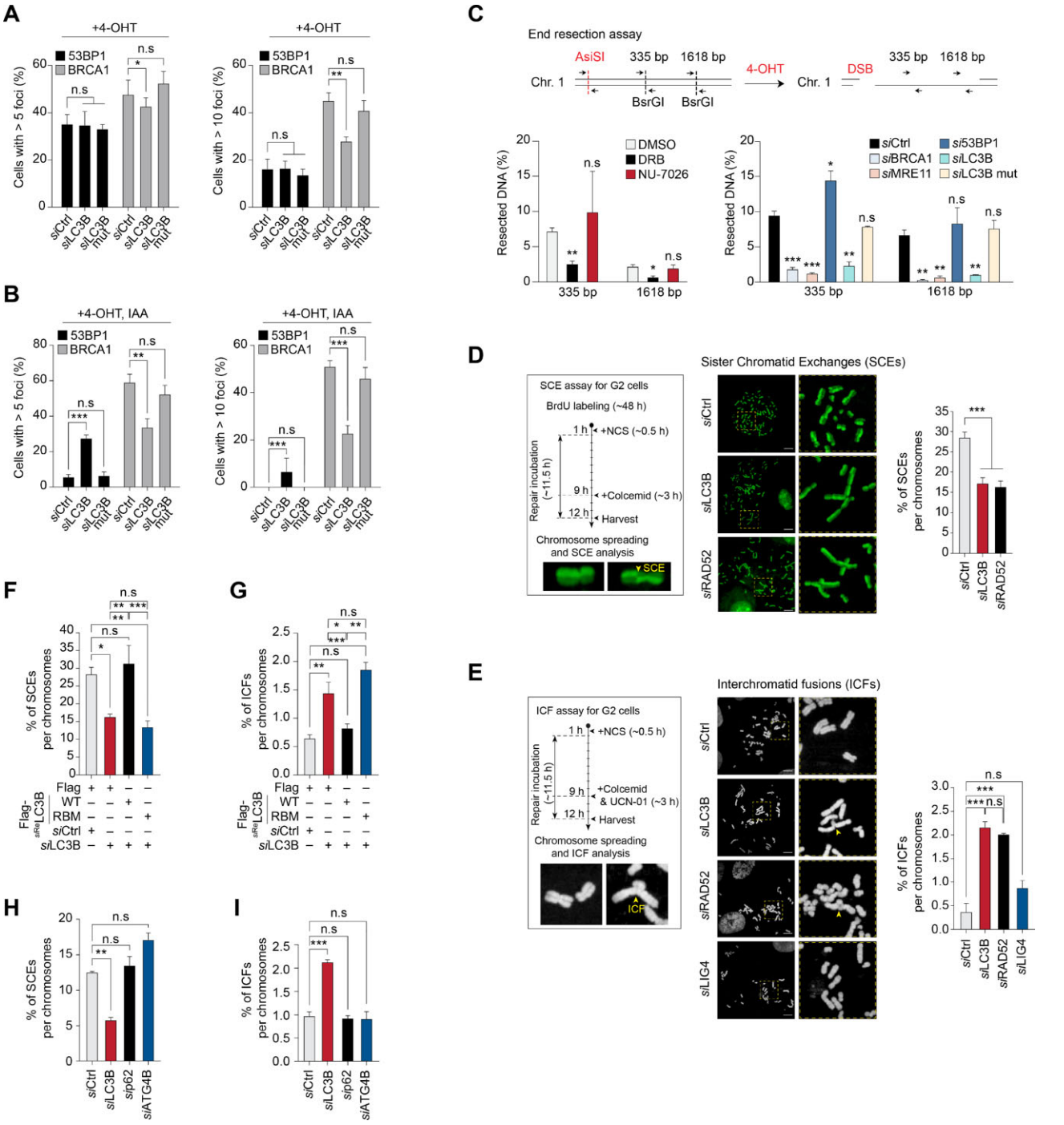

Figure 6. LC3B is a crucial factor to maintaining chromosomal integrity through TA-HRR. (**A**) Examination of 53BP1 and BRCA1 foci in an LC3B-depleted setting. *si*Ctrl: $n = 127$; *si*LC3B: $n = 213$; *si*LC3B mut: $n = 121$. (**B**) Post-IAA treatment in AID-DIvA cells shows an increase in 53BP1 foci, signifying a shift towards NHEJ under LC3B deficiency. *si*Ctrl: $n = 170$; *si*LC3B: n = 122; *si*LC3B mut: $n = 122$. (**C**) DNA end-resection assay in DIvA cells: The top panel provides a schematic representation, while the bottom panel quantifies ssDNA formation either 335 or 1618 bp downstream from the AsiSI-induced break. Data stem from cells treated with specific inhibitors (left panel) or transfected with the mentioned *si*RNAs (right panel) post-DSB initiation via 4-OHT. Based on $n = 6$ independent experiments. (**D**) Decline in SCE occurrences with LC3B deficiency. *si*Ctrl: $n = 732$; *si*LC3B: $n = 708$; *si*RAD52: $n = 777$. (**E**) Rise in ICF events upon LC3B knockdown, analogous to effects seen with RAD52 depletion. LIG4 depletion's impact is negligible. *si*Ctrl: $n = 525$; *si*LC3B: $n = 928$; *si*RAD52: $n = 598$; *si*LIG4: $n = 570$. (F and G) The drop in SCE (**F**) and surge in ICF (**G**) after LC3B knockdown were negated by reintroducing LC3B WT but continued with LC3B RBM. From left to right, n values are 607, 594, 846, 756, 495, 389, 331 and 307. (H and I) Knockdown of LC3B WT displays notable impacts on SCE (**H**) and ICF (**I**), contrasting with the insignificant changes observed with p62 and ATG4B knockdowns. From left to right: $n = 326$, 283, 329, 431, 144, 120, 276 and 118. For figures (A–I), Tukey's multiple comparisons test was utilized. Levels of significance: *, $P < 0.05$; **, $P < 0.01$; ***, $P < 0.001$; n.s., non-significant. Data are presented as mean ± s.e.m. All scale bars represent 10 μm.

accentuates its distinctive binding behavior. This hints at LC3B's RRM favoring single-stranded RNA (SSR) and DNA/RNA hybrids. Our nRIP-seq data corroborate LC3B's preference for AU-rich element sequences when binding SSR. However, such specificity seems lacking for hybrids. What underpins this selectiveness? Potential factors could include RNA or hybrid secondary structures, charge distributions, or post-transcriptional modifications such as 5hmC and m6A. Alternatively, structural variations in LC3B could dictate its binding predilections. Figure 5J displays diverse electrophoretic migration patterns for LC3B-SSR complexes, suggesting potential structural alterations in LC3B. Such changes might influence its affinity for SSR or hybrids, implying multiple interaction modalities.

We postulate that these interaction dynamics might be molded by alterations in LC3B's structure. While our deductions are drawn primarily from bioinformatics, they pave the way for subsequent targeted functional experiments. A comprehensive grasp of LC3B's structure and its interactions with diverse RNA forms is paramount for unraveling the intricacies of RNA biology.

Transitioning our focus, contemporary studies spotlight autophagy's extended influence on cellular mechanisms and genomic stability. Historically linked with cellular detoxification, the breadth and importance of autophagy's participation in DNA repair is increasingly recognized. For instance, ATG5 transcends its traditional autophagic role. Maskey *et al.* (46) linked ATG5 expression to chromosomal alterations after DNA damage. Demirbag-Sarikaya *et al.* (47) spotlighted ATG5's enhanced engagement with DNA repair proteins under genotoxic stress. Additionally, impaired autophagy resulting in p62 nuclear buildup restricts DSB repair through RNF168-mediated histone ubiquitination (48). Complementing this, Xu *et al.* (49) observed Beclin 1′s cooperation with DNA topoisomerase IIβ during occurrences of DSBs. Similarly, Yan et al. (50) delineated the joint function of nuclear LC3-II and phosphorylated Ulk1 with proteins crucial for preservation of genomic stability. Liu *et al.* (20) proposed that diminished autophagy efficiency might undermine robust HR DNA repair.

Building upon these foundational insights, our study reveals LC3B's notable impact on R-loop dynamics and genomic stability, further defining autophagy's involvement in DNA repair. The upsurge in R-loops consequent to a decrease in LC3B, as evidenced by our HR reporter assay data, underscores a critical role for LC3B not just in autophagic pathways but also in directly modulating the DNA damage response. Although our results do not confirm a direct interaction between LC3B and XPG, they point to a possible modulatory effect of LC3B on areas prone to R-loop formation, which could play a significant role in the stabilization of genomic sequences and facilitation of DNA repair. These findings enhance our understanding of LC3B's function within cellular defense mechanisms, suggesting a convergence of autophagy and DNA repair pathways that may inform novel therapeutic strategies to preserve genomic integrity.

Collectively, these investigations draw connections between autophagic modulators and DNA repair components. Our study, however, intimates a more direct correlation, suggesting LC3B may influence the mRNA regulation of DNA repair entities and even bind directly to R-loops to modulate TA-HRR. This work further solidifies the intimate ties between autophagy and DDR.

Yet, the converse relationship remains an enigma: how does LC3B's impact on TA-HRR influence autophagy? This query warrants deeper investigation. Still, our revelations help to fill existing knowledge gaps concerning disorders arising from the interplay of autophagy and DDR, presenting promise for new lines of therapeutic innovations.

Data availability

The nRIP-seq data supporting the findings of this study have been deposited in the NCBI's Gene Expression Omnibus and are accessible through the GEO Series at accession number GSE243991.

Supplementary data

Supplementary Data are available at NAR Online.

Acknowledgements

We wish to express our deep appreciation to Dr Roger A. Greenberg for his generous donation of the U2OS 2–6–3 and 2–6–5 reporter cell lines, which were instrumental for our FokI analysis. Additionally, our thanks go to Dr Gaelle Legube for providing the DIvA- and AID DIvA-U2OS cell lines (with stable AsiSI-ER expression), and to Dr Jeremy Stark for sharing the GFP-reporter cell lines essential for our DNA repair assays. We are also grateful to Dr Kiyoshi Miyagawa for supplying the pcDNA3.1-RNase H (M27), pEGFP-C1-RNase H (M27) and HBD plasmids, as well as RPE-hTERT WT cell line. Our appreciation extends to Dr Suhwan Chang and Dr Joohyuk Sohn for their contributions of the HA-BRCA1 and BRCA1-Myc-Flag plasmids, respectively.

Author contributions: J.Y., Y.H., H.Y., B.D.L. and H.C.K. conceived and designed the experiments. J.Y., Y.H. and H.Y. executed the majority of the experiments. J.M.C. and S.K. assisted with m-IR experiments. G.K. and Y.L. purified recombinant proteins and carried out the EMSA experiment. J.M.C. and S.K. provided further analysis of the immunofluorescence data. B.D.L. and H.C.K. engaged in in-depth discussions, provided comments, interpreted the data and wrote the paper.

Funding

National Research Foundation of Korea grant funded by the Korean government (MSIP) [NRF-2023R1A2C1005796]; Korea Health Technology R&D project of the Korea Health Industry Development Institute (KHIDI), funded by the Ministry of Health & Welfare, Republic of Korea [HR16C0001, HR22C1734]. Funding for the open access charge: National Research Foundation of Korea [NRF-2023R1A2C1005796].

Contact for reagent and resource sharing

Further information and requests for reagents may be directed to and will be fulfilled by the corresponding author, Ho Chul Kang, PhD; email: hckang@ajou.ac.kr.

Conflict of interest statement

None declared.

References

1. Aguilera,A. and Gomez-Gonzalez,B. (2008) Genome instability: a mechanistic view of its causes and consequences. *Nat. Rev. Genet.*, **9**, 204–217.
2. Ceccaldi,R., Rondinelli,B. and D'Andrea,A.D. (2016) Repair pathway choices and consequences at the double-strand break. *Trends Cell Biol.*, **26**, 52–64.
3. Huang,R. and Zhou,P.K. (2021) DNA damage repair: historical perspectives, mechanistic pathways and clinical translation for targeted cancer therapy. *Signal Transduct. Target Ther.*, **6**, 254.
4. Branzei,D. and Foiani,M. (2008) Regulation of DNA repair throughout the cell cycle. *Nat. Rev. Mol. Cell Biol.*, **9**, 297–308.
5. Hustedt,N. and Durocher,D. (2016) The control of DNA repair by the cell cycle. *Nat. Cell Biol.*, **19**, 1–9.
6. O'Driscoll,M. and Jeggo,P.A. (2006) The role of double-strand break repair - insights from human genetics. *Nat. Rev. Genet.*, **7**, 45–54.
7. Shrivastav,M., De Haro,L.P. and Nickoloff,J.A. (2008) Regulation of DNA double-strand break repair pathway choice. *Cell Res.*, **18**, 134–147.
8. Scully,R., Panday,A., Elango,R. and Willis,N.A. (2019) DNA double-strand break repair-pathway choice in somatic mammalian cells. *Nat. Rev. Mol. Cell Biol.*, **20**, 698–714.
9. Yasuhara,T., Kato,R., Hagiwara,Y., Shiotani,B., Yamauchi,M., Nakada,S., Shibata,A. and Miyagawa,K. (2018) Human Rad52 promotes XPG-mediated R-loop processing to initiate transcription-associated homologous recombination repair. *Cell*, **175**, 558–570.
10. Yasuhara,T., Kato,R., Yamauchi,M., Uchihara,Y., Zou,L., Miyagawa,K. and Shibata,A. (2022) RAP80 suppresses the vulnerability of R-loops during DNA double-strand break repair. *Cell Rep.*, **38**, 110335.
11. Hoeller,D., Hecker,C.M. and Dikic,I. (2006) Ubiquitin and ubiquitin-like proteins in cancer pathogenesis. *Nat. Rev. Cancer*, **6**, 776–788.
12. Dantuma,N.P. and van Attikum,H. (2016) Spatiotemporal regulation of posttranslational modifications in the DNA damage response. *EMBO J.*, **35**, 6–23.
13. Kim,S., Kwon,M., Hwang,Y., Yoon,J., Park,S. and Kang,H.C. (2021) Stress-induced NEDDylation promotes cytosolic protein aggregation through HDAC6 in a p62-dependent manner. *iScience*, **24**, 102146.
14. Vijayakumaran,S. and Pountney,D.L. (2018) SUMOylation, aging and autophagy in neurodegeneration. *Neurotoxicology*, **66**, 53–57.
15. Debnath,J., Gammoh,N. and Ryan,K.M. (2023) Autophagy and autophagy-related pathways in cancer. *Nat. Rev. Mol. Cell Biol.*, **24**, 560–575.
16. Jackson,S.P. and Durocher,D. (2013) Regulation of DNA damage responses by ubiquitin and SUMO. *Mol. Cell*, **49**, 795–807.
17. Schwertman,P., Bekker-Jensen,S. and Mailand,N. (2016) Regulation of DNA double-strand break repair by ubiquitin and ubiquitin-like modifiers. *Nat. Rev. Mol. Cell Biol.*, **17**, 379–394.
18. Eliopoulos,A.G., Havaki,S. and Gorgoulis,V.G. (2016) DNA damage response and autophagy: a meaningful partnership. *Front. Genet.*, **7**, 204.
19. Vessoni,A.T., Filippi-Chiela,E.C., Menck,C.F. and Lenz,G. (2013) Autophagy and genomic integrity. *Cell Death Differ.*, **20**, 1444–1454.
20. Liu,E.Y., Xu,N., O'Prey,J., Lao,L.Y., Joshi,S., Long,J.S., O'Prey,M., Croft,D.R., Beaumatin,F., Baudot,A.D., *et al.* (2015) Loss of autophagy causes a synthetic lethal deficiency in DNA repair. *Proc. Natl. Acad. Sci. U.S.A.*, **112**, 773–778.
21. Gomes,L.R., Menck,C.F.M. and Leandro,G.S. (2017) Autophagy roles in the modulation of DNA repair pathways. *Int. J. Mol. Sci.*, **18**, 2351.
22. Hewitt,G. and Korolchuk,V.I. (2017) Repair, reuse, recycle: the expanding role of autophagy in genome maintenance. *Trends Cell Biol.*, **27**, 340–351.
23. Mucino-Hernandez,G., Acevo-Rodriguez,P.S., Cabrera-Benitez,S., Guerrero,A.O., Merchant-Larios,H. and Castro-Obregon,S. (2023) Nucleophagy contributes to genome stability through degradation of type II topoisomerases A and B and nucleolar components. *J. Cell Sci.*, **136**, jcs260563.
24. Shanbhag,N.M., Rafalska-Metcalf,I.U., Balane-Bolivar,C., Janicki,S.M. and Greenberg,R.A. (2010) ATM-dependent chromatin changes silence transcription in cis to DNA double-strand breaks. *Cell*, **141**, 970–981.
25. Aymard,F., Bugler,B., Schmidt,C.K., Guillou,E., Caron,P., Briois,S., Iacovoni,J.S., Daburon,V., Miller,K.M., Jackson,S.P., *et al.* (2014) Transcriptionally active chromatin recruits homologous recombination at DNA double-strand breaks. *Nat. Struct. Mol. Biol.*, **21**, 366–374.
26. Munoz,M.C., Yanez,D.A. and Stark,J.M. (2014) An RNF168 fragment defective for focal accumulation at DNA damage is proficient for inhibition of homologous recombination in BRCA1 deficient cells. *Nucleic Acids Res.*, **42**, 7720–7733.
27. Prendergast,L., McClurg,U.L., Hristova,R., Berlinguer-Palmini,R., Greener,S., Veitch,K., Hernandez,I., Pasero,P., Rico,D., Higgins,J.M.G., *et al.* (2020) Resolution of R-loops by INO80 promotes DNA replication and maintains cancer cell proliferation and viability. *Nat. Commun.*, **11**, 4534.
28. Kim,J.J., Lee,S.Y., Hwang,Y., Kim,S., Chung,J.M., Park,S., Yoon,J., Yun,H., Ji,J.H., Chae,S., *et al.* (2021) USP39 promotes non-homologous end-joining repair by poly(ADP-ribose)-induced liquid demixing. *Nucleic Acids Res.*, **49**, 11083–11102.
29. Kitagawa,R., Niikura,Y., Becker,A., Houghton,P.J. and Kitagawa,K. (2023) EWSR1 maintains centromere identity. *Cell Rep.*, **42**, 112568.
30. Sharma,A.K., Fitieh,A.M., Hafez Ali,J.Y. and Ismail,I.H. (2022) Protocol to measure end resection intermediates at sequence-specific DNA double-strand breaks by quantitative polymerase chain reaction using ER-AsiSI U2OS cells. *STAR Protoc.*, **3**, 101861.
31. Tumini,E. and Aguilera,A. (2021) The sister-chromatid exchange assay in human cells. *Methods Mol. Biol.*, **2153**, 383–393.
32. Gibhardt,C.S., Roth,B., Schroeder,I., Fuck,S., Becker,P., Jakob,B., Fournier,C., Moroni,A. and Thiel,G. (2015) X-ray irradiation activates K+ channels via H2O2 signaling. *Sci. Rep.*, **5**, 13861.
33. Dikic,I. and Elazar,Z. (2018) Mechanism and medical implications of mammalian autophagy. *Nat. Rev. Mol. Cell Biol.*, **19**, 349–364.
34. Sun,L., Xiong,H., Chen,L., Dai,X., Yan,X., Wu,Y., Yang,M., Shan,M., Li,T., Yao,J., *et al.* (2022) Deacetylation of ATG4B promotes autophagy initiation under starvation. *Sci. Adv.*, **8**, eabo0412.
35. Rusten,T.E. and Stenmark,H. (2010) p62, an autophagy hero or culprit?*Nat. Cell Biol.*, **12**, 207–209.
36. Newhart,A., Rafalska-Metcalf,I.U., Yang,T., Joo,L.M., Powers,S.L., Kossenkov,A.V., Lopez-Jones,M., Singer,R.H., Showe,L.C., Skordalakes,E., *et al.* (2013) Single cell analysis of RNA-mediated histone H3.3 recruitment to a cytomegalovirus promoter-regulated transcription site. *J. Biol. Chem.*, **288**, 19882–19899.
37. Cramer,P. (2019) Organization and regulation of gene transcription. *Nature*, **573**, 45–54.
38. Chao,S.H. and Price,D.H. (2001) Flavopiridol inactivates P-TEFb and blocks most RNA polymerase II transcription in vivo. *J. Biol. Chem.*, **276**, 31793–31799.
39. Chang,J.Y. (1997) A two-stage mechanism for the reductive unfolding of disulfide-containing proteins. *J. Biol. Chem.*, **272**, 69–75.
40. Sollier,J. and Cimprich,K.A. (2015) Breaking bad: r-loops and genome integrity. *Trends Cell Biol.*, **25**, 514–522.
41. Bader,A.S. and Bushell,M. (2020) DNA:RNA hybrids form at DNA double-strand breaks in transcriptionally active loci. *Cell Death. Dis.*, **11**, 280.
42. Niehrs,C. and Luke,B. (2020) Regulatory R-loops as facilitators of gene expression and genome stability. *Nat. Rev. Mol. Cell Biol.*, **21**, 167–178.

43. Zong,D., Oberdoerffer,P., Batista,P.J. and Nussenzweig,A. (2020) RNA: a double-edged sword in genome maintenance. *Nat. Rev. Genet*., **21**, 651–670.
44. Marnef,A. and Legube,G. (2021) R-loops as Janus-faced modulators of DNA repair. *Nat. Cell Biol*., **23**, 305–313.
45. Saunus,J.M., French,J.D., Edwards,S.L., Beveridge,D.J., Hatchell,E.C., Wagner,S.A., Stein,S.R., Davidson,A., Simpson,K.J., Francis,G.D., *et al.* (2008) Posttranscriptional regulation of the breast cancer susceptibility gene BRCA1 by the RNA binding protein HuR. *Cancer Res*., **68**, 9469–9478.
46. Maskey,D., Yousefi,S., Schmid,I., Zlobec,I., Perren,A., Friis,R. and Simon,H.U. (2013) ATG5 is induced by DNA-damaging agents and promotes mitotic catastrophe independent of autophagy. *Nat. Commun*., **4**, 2130.
47. Demirbag-Sarikaya,S., Akkoc,Y., Turgut,S., Erbil-Bilir,S., Kocaturk,N.M., Dengjel,J. and Gozuacik,D. (2022) A novel ATG5 interaction with Ku70 potentiates DNA repair upon genotoxic stress. *Sci. Rep*., **12**, 8134.
48. Wang,Y., Zhang,N., Zhang,L., Li,R., Fu,W., Ma,K., Li,X., Wang,L., Wang,J., Zhang,H., *et al.* (2016) Autophagy regulates chromatin ubiquitination in DNA damage response through elimination of SQSTM1/p62. *Mol. Cell*, **63**, 34–48.
49. Xu,F., Fang,Y., Yan,L., Xu,L., Zhang,S., Cao,Y., Xu,L., Zhang,X., Xie,J., Jiang,G., *et al.* (2017) Nuclear localization of Beclin 1 promotes radiation-induced DNA damage repair independent of autophagy. *Sci. Rep*., **7**, 45385.
50. Yan,S., Liu,L., Ren,F., Gao,Q., Xu,S., Hou,B., Wang,Y., Jiang,X. and Che,Y. (2017) Sunitinib induces genomic instability of renal carcinoma cells through affecting the interaction of LC3-II and PARP-1. *Cell Death. Dis*., **8**, e2988.

Received: November 9, 2023. **Revised:** February 15, 2024. **Editorial Decision:** February 15, 2024. **Accepted:** February 19, 2024